



Final Report:

Study and Analysis of the Transition Between Vertical and  
Horizontal Flight in Tilt Rotor Drones to Increase Efficiency of  
Power Consumption



Final Report:  
Study and Analysis of the Transition Between Vertical and  
Horizontal Flight in Tilt Rotor Drones to Increase Efficiency of  
Power Consumption

April 18, 2023  
Team #9

Prepared by M-Tilt Team Members:

Joshua Chapp  
Noah Kinnucan  
William Loomis  
Nicholas Mellanby  
Bryan Rodwell  
Alexandra Strehlow

Prepared for:  
Professor Jack Fishstrom  
Professor Thomas Miller

# Table of Contents

<b>List of Figures</b>	<b>3</b>
<b>List of Tables</b>	<b>5</b>
<b>Definitions of Abbreviations, Acronyms, and Symbols</b>	<b>6</b>
<b>Executive Summary</b>	<b>8</b>
<b>1. Introduction</b>	<b>9</b>
1.1 Tilt Rotor Drone Overview	9
1.2 Justification and Existing Literature	11
1.3 Organizational Preview	11
<b>2. Proof of Qualifications</b>	<b>11</b>
<b>3. Requirements</b>	<b>12</b>
3.1 Full Aircraft Design	12
3.2 Structural Reliability	12
3.3 Avionics System	12
3.4 Peak Power and Energy Consumption Minimization	13
<b>4. Test Article Design</b>	<b>13</b>
4.1 Wing Section	13
4.1.1 Wing Sizing and Airfoil Choice	13
4.1.2. Wing Materials and Manufacturing	14
4.2 Propulsion System	14
4.3 Tilt Mechanism	14
4.4.1 Design Considerations	15
4.4.2 Servo Mount	15
4.4.3 Motor Mount	16
4.4.4 Software and Electronics	16
<b>5. Design Validation</b>	<b>17</b>
5.1 Phase 1 - Propulsion System Static Testing	17
5.2 Phase 2 - Propulsion System Dynamic Testing	19
5.3 Phase 3 - Wing Aerodynamic Performance Testing	20
5.4 Tilt Mechanism Functionality Testing	23
<b>6. Simulation</b>	<b>24</b>
6.1 Model Overview	25
6.2 Simulation Results	26
6.2.1 Transition Profile Shape	26
6.2.2 Transition Profile Duration	29
<b>7. Simulation Validation Testing</b>	<b>31</b>
7.1 Test Procedure	31
7.2 Test Results	32
<b>8. Project Schedule and Budget</b>	<b>33</b>

<b>9. Conclusions and Recommendations</b>	<b>35</b>
<b>Appendix A - Project Manager Nicholas Mellanby's Prototype Tilt Rotor Drone</b>	<b>36</b>
<b>Appendix B - Wing Section Manufacturing Methods</b>	<b>42</b>
<b>Appendix C - Tilt Rotor Mechanism FEA Studies</b>	<b>44</b>
<b>Appendix D - Tilt Mechanism Software Code</b>	<b>46</b>
<b>Appendix E - Phase 2 Pitot Probe Mounting Procedure</b>	<b>49</b>
<b>Appendix F - Wing Performance Testing Raw Data</b>	<b>50</b>
<b>Appendix G - Airfoil Performance Simulation</b>	<b>54</b>
<b>Appendix H - Simulink Model State Space</b>	<b>55</b>
<b>Appendix I - Step Function Transition Profiles</b>	<b>56</b>
<b>Appendix J - Changing Slope Transition Profiles</b>	<b>58</b>
<b>Appendix K - Complete State Space of 8 Second Linear Transition</b>	<b>60</b>
<b>Appendix L - Itemized Budget Breakdown</b>	<b>61</b>
<b>References</b>	<b>62</b>

## List of Figures

Figure 1.1: Tilt Rotor VTOL Drone Configuration	9
Figure 1.2: Example Tilt Rotor Drone Transition Profile	10
Figure 4.1: Wing Section Test Article	13
Figure 4.2: NACA 24012 2-D Airfoil Cross Section	13
Figure 4.3: Tilt Rotor Mechanism	15
Figure 4.4: Electronics Setup (View from Bottom of Spar)	16
Figure 4.5: Electronics Setup (View from Top of Spar)	17
Figure 5.1: Phase 1 Testing Set-Up using TYTO Thrust Stand	18
Figure 5.2: Phase 1 Testing Shows that Propulsion System Meets Requirements	18
Figure 5.3: Dynamic Thrust Test Setup	19
Figure 5.4: Propeller Efficiency	20
Figure 5.5: Wing Performance Test Setup	20
Figure 5.6: Wing Lift Characterization	21
Figure 5.7: Wing Drag Characterization	22
Figure 5.8: Wing Pitching Moment Characterization	22
Figure 5.9: Tilt Mechanism Load Test Setup	23
Figure 6.1: VTOL Drone Transition Simulink Model	24
Figure 6.2: Example Simulink Servo Tilt Profile	25
Figure 6.3: Simulated Transition Profile Functions	26
Figure 6.4: Power Consumption for Simulated Transition Profiles	27
Figure 6.5: Power Consumption of Varying Duration Linear Transitions	29
Figure 6.6: Peak and Total Power Consumption of Varying Duration Linear Transitions	30
Figure 7.1: Simulated and Tested Transition Profiles for Linear Tilt Input	31
Figure 8.1: Project Gantt Chart	32
Figure 8.2: Cumulative Hours Spent on Project	33

Figure A.1: Isometric View of Tilt Rotor Drone Prototype Assembly	36
Figure A.2: NACA 24012 Airfoil with Spaces for Support Structure and Electronics	36
Figure A.3: Wing Structure and Tilting Mechanism	38
Figure A.4: Prototype Drone During Wing Monokoting	39
Figure A.5: Full Prototype on Display at The University of Michigan Design Expo	40
Figure B.1: Prototype Composite Wing Section	42
Figure B.2: Webbing Effect on MonoKote Wing	43
Figure B.3: Balsa Sheet Structure in MonoKote Wing	43
Figure C.1: FEA Transition Stress and Deflection Analysis of Servo Mount	44
Figure C.2: FEA Transition Stress and Deflection Analysis of L Bracket	45
Figure E.1: Exit Airspeeds Behind the Propeller-Motor System	49
Figure G.1: $C_l$ vs. Alpha for Simulated Airfoil	54
Figure G.2: Simulated Drag Polar	54
Figure I.1: Simulated Step Profile Tilt and Power Profiles	56
Figure I.2: Simulated Intense Step Profile Tilt and Power Profiles	56
Figure J.1: Simulated Concave Up Slope Change vs Linear	58
Figure J.2: Simulated Concave Down Slope Change vs Linear	59
Figure K.1: Linear Transition Complete State Space	60

## List of Tables

Table 1.1: Tilt Rotor Drone Flight Mode Configurations	10
Table 6.1: Peak and Total Power Consumption for Simulated Transition Profiles	28
Table 9.1: Simplified Proposed vs. Final Budget Breakdown	33
Table C.1: Servo Mount FEA Results	45
Table F.1: Wing Performance Testing Raw Data (5 m/s)	50
Table F.2: Wing Performance Testing Raw Data (10 m/s)	51
Table F.3: Wing Performance Testing Raw Data (15 m/s)	52
Table F.4: Wing Performance Testing Raw Data (20 m/s)	53
Table L.1: Itemized Budget Breakdown	61

## Definitions of Abbreviations, Acronyms, and Symbols

$\alpha$	Angle of Attack
$^{\circ}$	Degrees
A	Ampere
AoT	Angle of Tilt
CA	Cyanoacrylate
$C_D$	Drag Coefficient
$C_L$	Lift Coefficient
$C_M$	Pitching Moment Coefficient
CNC	Computer Numerical Control
DAS	Data Acquisition System
DC	Direct Current
ESC	Electronic Speed Controller
FEA	Finite Element Analysis
ft	Foot
in.	Inch
kg	Kilograms
kg-cm	Kilogram-Centimeter
lbs	Pounds
kV	Kilovolt
LiPo	Lithium Polymer
m/s	Meters Per Second
mm	Millimeter
MPa	Megapascal
ms	Milliseconds
N	Newtons



PLA	Polylactic Acid (3D Printing Material)
PM	Project Manager
PWM	Pulse Width Modulation
T/W	Thrust-to-Weight ratio
USB	Universal Serial Bus
V	Volts
VTOL	Vertical Takeoff and Landing
W	Watts

## Executive Summary

The large power consumption of vertical takeoff and landing (VTOL) drones during their transition from vertical to horizontal flight limits performance parameters such as payload weight, range, and endurance. As VTOL drones become more prevalent in both the commercial and military sectors, this transition process must become more power efficient. Our team designed, built, and tested a tilt rotor half-wing test article to study VTOL transition and observe trends in power consumption. In this report, we present the results of our study of the transition between vertical and horizontal flight in tilt rotor drones to increase efficiency of power consumption.

Upon the completion of our study, we found that no one specific transition profile could be used to completely optimize power consumption; rather, a tradeoff must be made between minimizing total power consumption and minimizing peak power consumption based on the particular application of a specific vehicle. Our study consisted of multiple phases of design, analysis, testing, and data collection and was completed by six undergraduate students over the course of 16 weeks with a material budget of \$500.00. After defining design requirements based on a variety of factors including our Project Manager's (PM) design of a full vehicle, we developed the various components of our test article—a wing section, a propulsion system, and a tilting mechanism. The wing section uses a NACA 24012 airfoil and has a chord length of 10 inches (in.) and a span of 19 in. It is made of laser-cut balsa wood ribs with a square steel spar, and it is wrapped in a combination of balsa wood and MonoKote. The propulsion system uses an EMAX MT-3110 700 kilovolt (kV) brushless motor, a 60 ampere (A) electronic speed controller (ESC), and a 9 in.-by-4.5 in. Master Airscrew tri-blade propeller. The tilt mechanism consists of mounts for both a servo and a motor in addition to related control software. Using data collected during component testing, we developed a simulation that models the conditions and forces during the transition from vertical to horizontal flight for a VTOL tilt rotor drone. Wind tunnel testing of the fully integrated test article—including the wing section, the propulsion system, and the tilting mechanism—provided data that was compared to the simulation and used to validate its accuracy. This testing showed that the simulation underestimates the peak power by ~30%, but the general behavior of the power consumption curve is accurate, especially after this peak. Future improvements to our test article and simulation will improve this result and allow us to better understand the tradeoff between minimizing peak power consumption and minimizing total power consumption.

## 1. Introduction

The purpose of this document is to formally publish our study of the transition between vertical and horizontal flight in tilt rotor drones to increase efficiency of power consumption. Currently, these drones are quite inefficient in their power consumption during their transition from vertical to horizontal flight. Our team investigated this problem by recreating the tilt rotor drone's transition phase through the use of our tilt rotor and wing test article. The results of this study will allow drone designers to create more power-efficient tilt rotor vehicles by leveraging the reduced power consumption transition profiles that this document presents. By reducing the power consumption, the required size of the power plant would decrease, allowing in exchange for increased payload, range, and endurance, all of which are positive characteristics of any aircraft. This report will describe in detail the background and justification of the study, the qualifications of the M-Tilt team, and the project description, including all facilities, materials, test articles, test procedures, simulations, and collected data deliverables.

### 1.1 Tilt Rotor Drone Overview

VTOL drones have a variety of uses as they are able to loiter over an area, take off and land from confined spaces, and demonstrate the range and speed of a fixed-wing aircraft. This unique ability makes them especially desirable for benefactors such as emergency services, agriculture, the military, and the general hobbyist. One common VTOL configuration is the tilt rotor (Figure 1.1), which has wingtip mounted propellers which rotate about the wing from vertical to horizontal, providing upward or forward thrust.

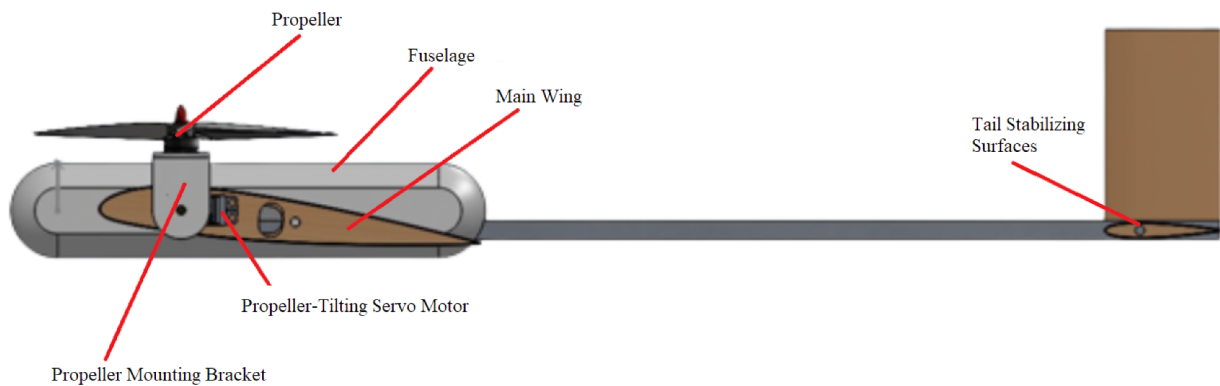





Figure 1.1: Tilt Rotor VTOL Drone Configuration Designed by PM

Table 1.1 shows how a tilt rotor drone's configuration, tilt angle, and horizontal speed changes throughout each of its flight modes: vertical takeoff/landing, transition, and cruise. It is important to note that in this table, and throughout future sections of this report, a 90 degree ( $^{\circ}$ ) tilt angle corresponds with an upward vertical motor orientation and  $0^{\circ}$  corresponds with a forward horizontal motor configuration.

Additionally, mentions of cruise speed refer to a speed of 15 meters per second (m/s), while mentions of max speed refer to a speed of 20 m/s.

Table 1.1: Tilt Rotor Drone Flight Mode Configurations

Flight Mode:	Vertical Takeoff/landing	Transition	Cruise
Configuration:			
Motor Tilt Angle (°):	90	90 to 0	0
Horizontal Velocity (m/s):	0	0 to Cruise Speed	Cruise Speed to Max Speed

At present, tilt rotor drones have a great deal of variance in how they conduct their transition phase between vertical and horizontal flight. The transition flight mode is quite complex as it requires a combination of motor tilt angles and motor power that not only maintain the drone’s altitude but also increase its horizontal velocity to its cruise speed. This relationship between motor tilt angles and motor power is deemed the transition profile. It is worth briefly noting that two other terms will be used in this report. The ‘tilt profile’ is the relationship between tilt angles and time, and the ‘power profile’ is the relationship between power consumption and time. Figure 1.2 below shows an example transition profile and how motor tilt angle and motor power are related. Notice that the motor consumption increases during the flight mode transition and is much greater than both the vertical configuration and the horizontal configuration. The figure below is just one example, but the shape of this transition profile can change greatly based on how the motor tilting motion is implemented. With respect to time, the motor tilt angle can rotate linearly from 90° to 0°, but it can also take other paths such as a cosine or exponential shape. These different transition methods all correspond to different peak power consumptions, total power consumptions, and profile shapes.

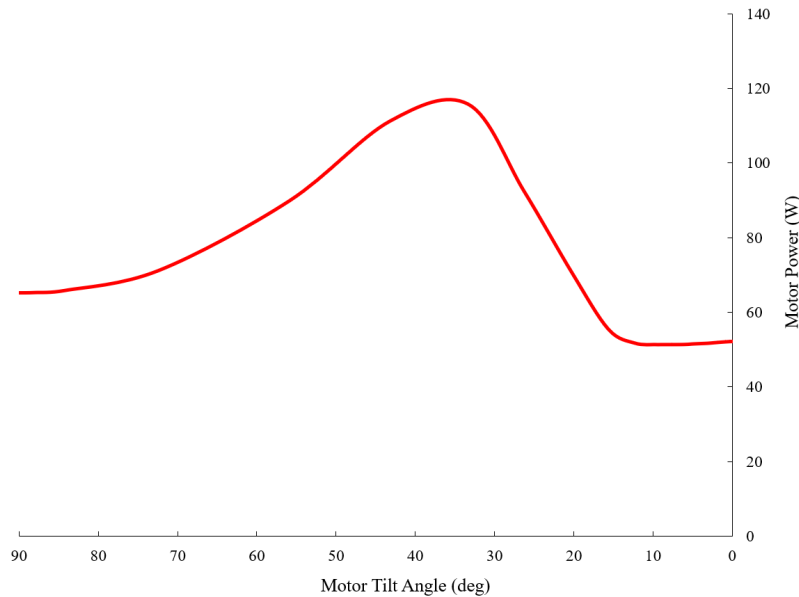


Figure 1.2: Example Tilt Rotor Drone Transition Profile

## **1.2 Justification and Existing Literature**

In recent years, drones have become an increasingly useful tool in a variety of industries. For example, they are quite practical for search and rescue missions, forest fire monitoring, and crop management, just to name a few. These applications require drones with a long endurance to monitor the largest area possible, as well as VTOL capabilities to allow for operation in areas with a confined takeoff space. These requirements are most suited by drones that can transition from vertical flight in VTOL to horizontal flight in cruise. Additionally, mission profiles for a tilt rotor drone may require multiple transitions from vertical to horizontal flight, hence why studying the transition is relevant and important. Many companies and academics are investigating such drones and working on optimizing their configurations; however, there is still a great deal of information needed to advance their designs.

While company research is proprietary, our team referenced numerous scholarly articles to gain a broader understanding of the general field of VTOL aircraft. Subjects of these articles included VTOL tail-sitter unmanned aerial vehicles (UAVs) [2], VTOL UAVs with more advanced control systems employing machine learning and neural networks [4,5], and battery-powered VTOL UAVs [7]. Other research teams also attempted to model the aerodynamics of VTOL transition [8,9]. Our study, of course, focuses on the tilt rotor VTOL configuration; however, each of these sources showed us the types of testing and analysis to be expected from our study, and they proved just how much there is to explore in this area. Our study will further the growing research on VTOLs in general, and the findings will enable drone designers to implement this configuration and trade power plant weight for improved payload, range, and endurance.

## **1.3 Organizational Preview**

This report is composed of nine main sections along with preface material, a list of references, and appendices. The first main section is the introduction concluding with this organizational preview. The second is a brief discussion of our team's qualifications for this project. The third section details the criteria for success and requirements of our project. The fourth is a description of the design and construction of our wing test article. Following this is a description of the tests conducted to validate the performance of our test article components. The sixth section is a discussion of our simulation of a full aircraft, the requirements of which drove the design of our test article. This section is followed by a description of the testing used to validate our simulation. The eighth section is a breakdown of our budget. Finally, our report ends with a conclusion of our findings and recommendations for future VTOL transition methods.

## **2. Proof of Qualifications**

The M-Tilt team is qualified to conduct this study because of the great deal of experience and knowledge we possess being aerospace engineering students attending one of the most prestigious universities in the country. Additionally, members of our team have prior extracurricular experience building and flying small drones with University of Michigan project teams such as Michigan Sustainability Applications for Aerospace Vehicle Engineering (M-SAAVE) and Michigan Vertical Flight Technology (MVFT). Our team also relied on additional assistance throughout the project, which is why we kept in contact with professors within the University of Michigan's Department of Aerospace Engineering as necessary for

guidance and clarification. These professors were able to provide the necessary support across a wide range of fields such as hardware, software, and fabrication.

### **3. Requirements**

In order to set an appropriate scope for our investigation into the transition for tilt-rotor drones, we outlined requirements and defined criteria that were used to evaluate the success of our test article and experiment. The requirements are based on the PM's full aircraft design, structural reliability of the test article, the avionics system, and the results of the final validation testing.

#### **3.1 Full Aircraft Design**

The high-level performance requirements were set based on our PM's small bi-rotor drone. The required weight is 1.1 kilograms (kg) (10 Newtons (N)), and it must have a thrust-to-weight ratio (T/W) of 1.4 consistent with that of larger VTOL aircraft. Therefore, our test article that emulates one-half of the drone must have a wing section that produces 0.55 kg of lift at cruise speed and the propulsion system must generate maximum thrust of 7 N. Moreover, the full system must be able lift the required weight of 0.55 kg using a combination of wing-generated lift and vectored thrust during the transition period such that no altitude is lost during transition. The criteria used to evaluate the success of our test article were based on our article meeting the thrust and lift requirements in testing conditions. More information on the full aircraft can be found in Appendix A.

#### **3.2 Structural Reliability**

In order to be comparable to flight-rated tiltrotor devices, our test article must be able to survive reasonable stress and forces encountered by a tiltrotor aircraft. The tilting servo motor must be able to provide enough torque to rotate the propeller under adverse weather conditions, rated for twice the provided thrust of the propeller. The wing and spar must also be able to support the load of the propeller and adverse wind conditions. Although this test article is only expected to see fewer than 100 stress cycles, the full flight article must be designed to have a longer life expectancy. Our criteria for success was that the test article did not fail during testing nor would it be expected to fail in its estimated lifetime.

#### **3.3 Avionics System**

It is very important for the success of our project that the avionics system is operating as intended. The requirements of our avionics system are that it must be able to accurately set the motor power and the servo attitude that sets the angle of our tilt mechanism. The criteria we used to evaluate the success of this requirement was if the servo could accurately actuate the tilt mechanism to tolerances of  $\pm 1^\circ$ , and that it could set the thrust of the motor to discrete values. Another requirement is that the system has the appropriate sensors and is able to record and display information about tilt angle and power draw. The criteria for success was if we were able to implement these sensors and record the required data.

### 3.4 Peak Power and Energy Consumption Minimization

For our final deliverable, we aimed to deliver an optimized profile for a small tilt-rotor drone transition that minimizes both peak power requirement and total energy consumption during transition. Our criteria for success was if we could recommend one profile that achieved both goals for optimizing a tilt profile.

## 4. Test Article Design

In this section, we describe our test article which consists of a wing section with an integrated propulsion system and tilt-mechanism. Along with an overview of each component, there are also a variety of discussions around the design choices and how they relate to theoretical calculations and analysis performed before building the test article.

### 4.1 Wing Section

The wing section is the primary lifting device of our test article during horizontal flight. The size and shape of the wing section was determined based on traditional sizing methods, as well as computer simulations of performance. The wing section is shown below in Figure 4.1 with important components labeled.

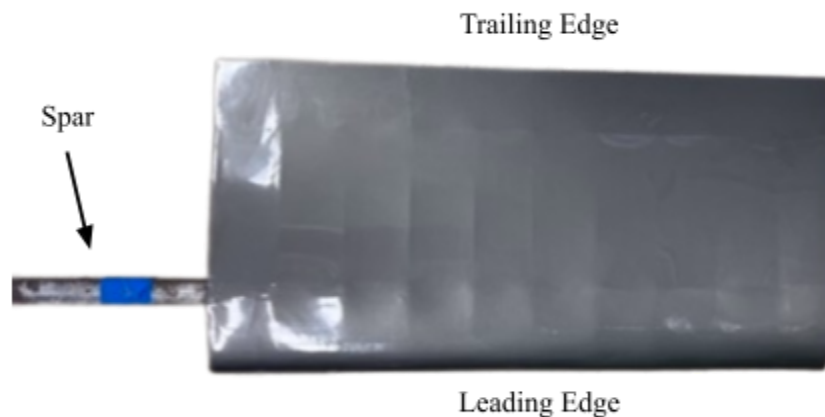


Figure 4.1: Wing Section Test Article

#### 4.1.1 Wing Sizing and Airfoil Choice

The main driver for our wing design was that it must produce 5 N of lift in cruise conditions, which represents one-half of the PM's aircraft. Initial research led us to select a NACA 24012 profile for our airfoil. We chose this airfoil because it has a small camber, which makes adding hardware easier, and because simulations showed that it could produce our desired lift at small angles of attack (Figure 4.2). Another constraint for wing sizing is that the cross section must be wide enough to support the servo and other mounting hardware for the tilting mechanism. Based on the expected size of our servos, we set the maximum thickness of the airfoil to 1.2 in., which meant the wing needed a 10 in. chord. In order to produce a lift of 5 N, we calculated our test airfoil would need to have a 19 in. span.

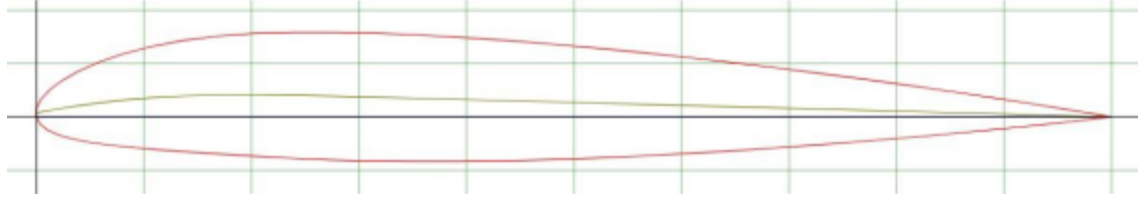


Figure 4.2: NACA 24012 2-D Airfoil Cross Section

#### 4.1.2. Wing Materials and Manufacturing

For our final test article, the wing section was fixed to a steel spar. The wing section contained 10 laser-cut birch plywood ribs with 1/32 in. contoured balsa sheets around the leading and trailing edge. To create a smooth upper and lower surface, MonoKote covering was adhered to the wooden structure. Mounting hardware for the tilting mechanism was embedded in the wing section and reinforced with a doubled rib and aluminum sheet metal. For more details on manufacturing methods, refer to Appendix B.

### 4.2 Propulsion System

We used simulations in our project to predict the performance of our propulsion system throughout a flight profile and to predict the performance of the wing section. The propulsion system that provided the required 7 N of lift includes an EMAX MT-3110 electric motor, a 3-cell LiPo battery, a Skywalker 60A ESC, with a 9-in diameter 3-bladed Master Airscrew propeller. We used thrust-disk propeller theory to determine the airspeeds that the propeller could generate in static conditions at different power inputs. We used Equation 1 to determine a baseline cruise velocity that would be used in further testing. In Equation 1,  $\rho$  is the air density,  $A_d$  is the disk area,  $U_e$  is the exit velocity, and  $U_o$  is the incoming flow speed.

$$T = \frac{\rho A_d}{2} [U_e^2 - U_o^2] \quad (1)$$

Based on our 9 in. diameter propeller and estimating performance at sea level where  $U_o = 0$  m/s, we determined that the target cruise velocity for stable level flight would be approximately 15 m/s. We decided to compare the accelerated airspeed against the power supplied to the motor and propeller since the goal final deliverable is to minimize power. Thus, we wanted to determine where the accelerated flow vs. power curve began to level off, which gives us a power setting for the most efficient cruise.

### 4.3 Tilt Mechanism

The tilt rotor mechanism consists of three main components: the 20 kilogram-centimeter (kg-cm) servo, the servo mount, and the 3D printed L bracket. The 20 kg-cm digital servo was chosen due to its strength and availability. The servo itself did not need to be altered and only required the addition of a servo mount and L bracket. The entire tilt rotor mechanism can be seen below in Figure 4.3 with the relevant components labeled.



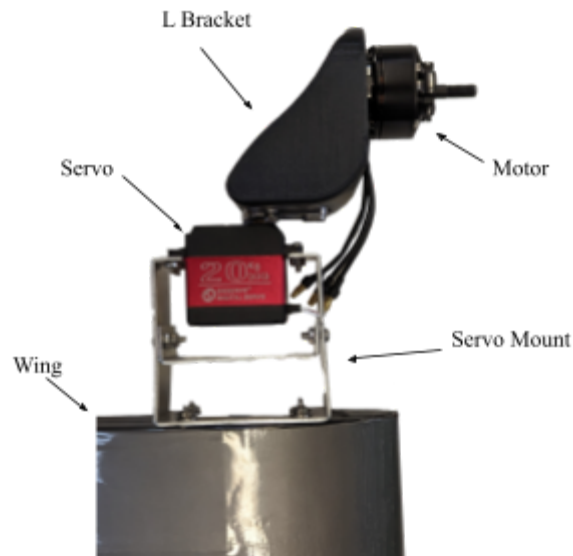


Figure 4.3: Tilt Rotor Mechanism

#### 4.4.1 Design Considerations

Throughout the design of this mount, its strength, weight, accessibility, and propeller wake blockage were all major considerations. To ensure the part had the required strength to not break nor deflect under the loads in the wind tunnel while also maintaining a relatively low weight, aluminum and high infill 3D printed materials were used. Additionally, finite element analysis (FEA) studies were conducted on these components which also helped to maximize strength and decrease weight. These simulations can be seen in Appendix C. In terms of placement, our team considered implementing the servo inside the wing which would have decreased the drag, but ultimately decided to implement the entire mechanism outside the wing to allow our team to make adjustments and replace components if necessary. This decision increased propeller blockage as well, but our team believed the ability to easily access our mechanism was more important than slightly increased propeller blockage due to the possibility of component failure or other unforeseen circumstances. Moreover, the horizontal and vertical cross sections were still minimized as much as possible to decrease the propeller blockage.

#### 4.4.2 Servo Mount

The servo mount is a C-shaped metal bracket that was fitted and designed to be able to hold the servo fixed and to be easily mountable to the wing. The bracket was constructed out of 1/16 in. thick aluminum sheet metal. This sheet metal was chosen based on its availability and thickness. The part consists of two main pieces, being the main C-shaped bracket and the mount support which spans through the center of the bracket. The mount support was included to prevent the main bracket from deflecting and bending during cruise. The two pieces were constructed separately to ease the manufacturing process, which consisted of hole punching and metal stamping. These two pieces were then assembled using screws. Additional screws and washers were then used to mount the servo mount to the wing article.

### 4.4.3 Motor Mount

The L bracket used to connect the motor to the servo is a 3D printed component made out of polylactic acid (PLA), which is a very common 3D printing filament. This part was 3D printed because it allowed for more complex truss supported geometry that ultimately increased the strength while maintaining a low weight. Additionally, the 3D printing allowed for the bracket to be further customized in a way that would decrease propeller blockage and align with our desired shape and size. To then actually print the L bracket our team adjusted the 3D print settings to increase the parts strength, such as increasing the part's infill and outer layer thickness.

### 4.4.4 Software and Electronics

Wind tunnel testing requires the ability to control everything on the test article precisely from outside the tunnel. With this in mind, we made sure to spend ample time designing and iterating on our electronics setup. The motor and servo are controlled using an Arduino Uno board connected via universal serial bus (USB) to a laptop, with power for the servo coming from a AA battery pack providing 6 volts (V) and power for the motor coming from a direct current (DC) power supply set to a constant voltage of 16.8 V to replicate a 4-cell lithium polymer (LiPo) battery. An overview of this setup is shown below in Figures 4.4 and 4.5.

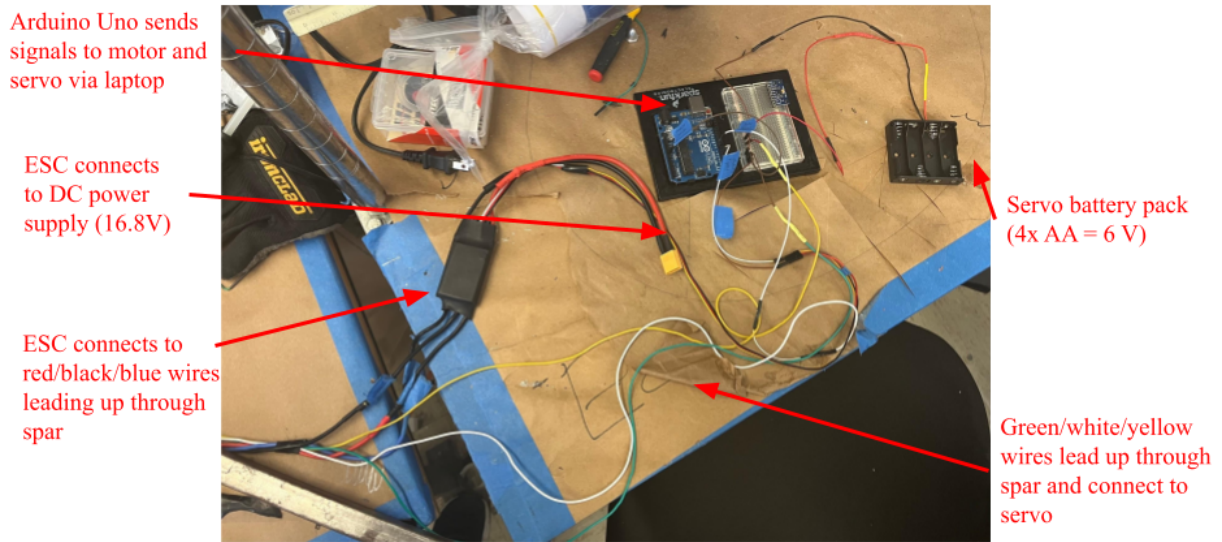


Figure 4.4: Electronics Setup (View from Bottom of Spar)

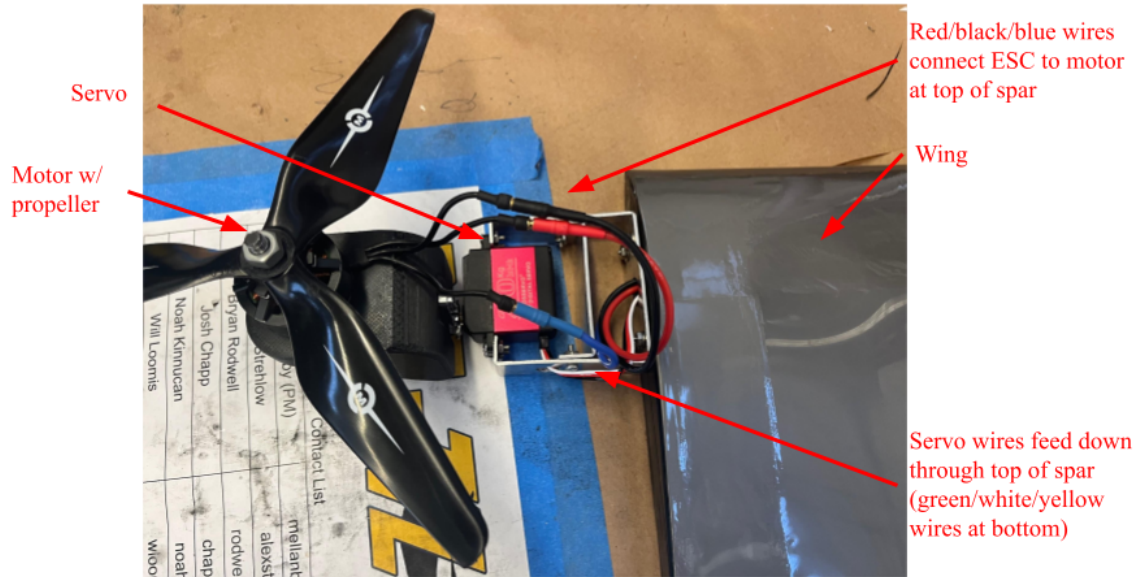


Figure 4.5: Electronics Setup (View from Top of Spar)

Using the serial monitor in the Arduino software, we were able to send commands to both the servo and the motor simultaneously. For example, an input of <90, 50> rotates the servo to the 90° position while setting the motor to 50% throttle via the ESC. The software also addresses a variety of issues, such as calibrating the servo position prior to any user input and mapping user inputs to pulse width modulation (PWM) values based on the specification of each component. Each input sends a PWM to the servo and motor; the servo only requires the pulse to be sent until it reaches the desired angle, while the motor requires this pulse to be sent constantly since brushless motors use the pulses to generate a magnetic field with internal coils and cause the propeller to spin. Servo inputs are between 500 and 2450 milliseconds (ms), which corresponds to a 270° range of motion; motor inputs are between 1000 and 2000 ms and are more arbitrary than those of the servo, as this range can be set in the Arduino code and programmed directly to the ESC. For a more detailed look at the Arduino code, see Appendix D. Since our software allows us to set specific thrust values to the motor as a percentage of full throttle, we determined that our test article meets software reliability requirements.

## 5. Design Validation

In this section, we relate the actual performance of our test article and individual components with their expected performance. It was important for us to perform each of these tests in order to fully characterize how a full-scale aircraft would perform for our simulation based on how well our test article validated the results from our simulations and preliminary research.

### 5.1 Phase 1 - Propulsion System Static Testing

In order to meet our requirement for 7 N of maximum thrust, we tested our chosen propulsion system to ensure that it could produce the required thrust. In Phase 1, the Propulsion System Characterization, success was based on if the combination of propeller, ESC, motor, and battery could produce at least 7 N of thrust repeatedly and reliably without causing damage to electronics or structural components. In order

to determine if the selected system could meet this criterion, the propulsion system was installed in the TYTO Robotics Thrust Stand with RC Benchmark software (Figure 5.1).

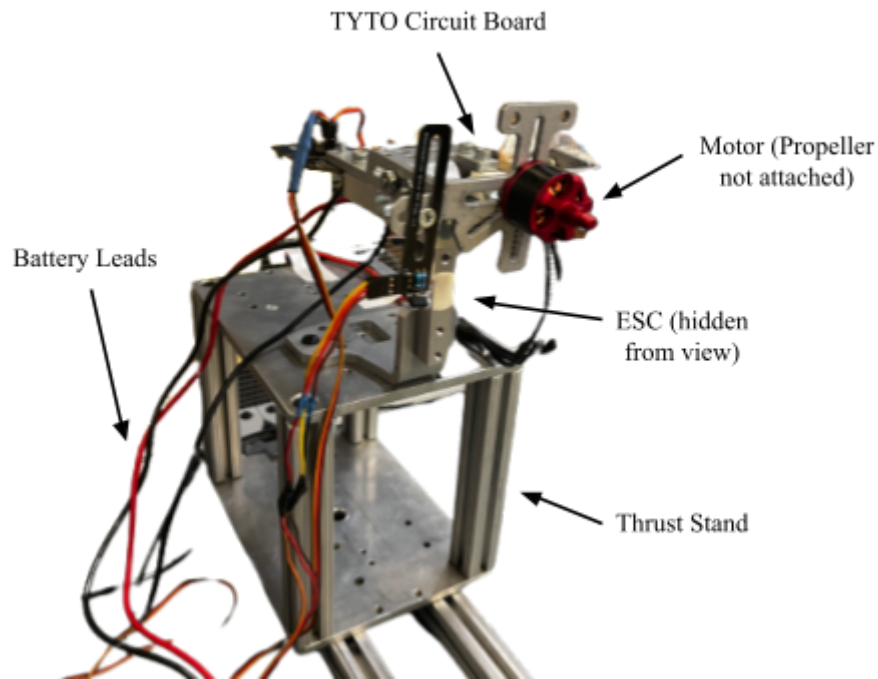


Figure 5.1: Phase 1 Set-Up using TYTO Thrust Stand

Both 3-cell and 4-cell LiPo batteries were tested, along with multiple motor and propeller combinations. This characterization of thrust vs. power was also used for our full aircraft simulation. Although both the 3-cell and 4-cell LiPo battery were both successful at generating the required thrust, we chose the 4-cell battery since it was in better condition than the 3-cell batteries. Based on results from Phase 1, the propulsion system consists of an EMAX MT-3110 motor, 4-cell LiPo battery, 60A ESC, and a 9-in. diameter 3-blade propeller was able to succeed in all criteria for this requirement. The results from Phase 1 are shown below in Figure 5.2.

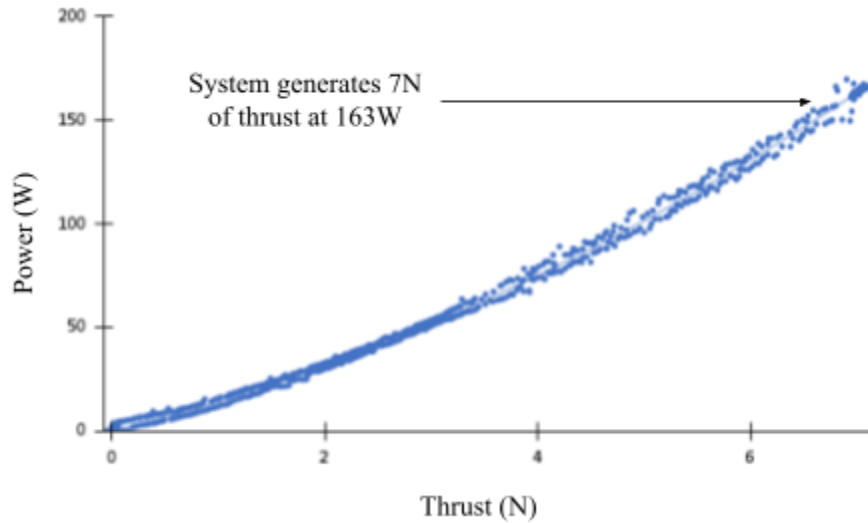


Figure 5.2: Phase 1 Testing Shows that Propulsion System Meets Requirements

### 5.2 Phase 2 - Propulsion System Dynamic Testing

Characterizing propeller thrust in a static environment is significant in predicting test article behavior at low airspeeds. However, dynamic characterization of the propeller-motor combination is also required to inform performance decisions at higher airspeeds. Propeller theory suggests that a given propeller will decrease in efficiency as freestream velocity increases. To validate this relationship, the same propeller thrust stand used in Phase 1 (Section 5.1) was mounted into the 2 ft-by-2 ft wind tunnel. A second Pitot probe in addition to the existing probe recording freestream velocity was mounted behind the propeller to record exit airspeed. For more information on the Pitot probe mounting, see Appendix E. The Phase 2 setup is shown in Figure 5.3 below.



2nd manually inserted Pitot probe

Figure 5.3: Dynamic Thrust Test Setup

The propeller-motor configuration was incrementally throttled from 0 Watts (W) to full power at freestream airspeeds of 0 m/s, 4 m/s, 8 m/s, 12 m/s, and 16 m/s. Freestream and exit airspeeds were recorded using the Pitot probes, while thrust and power draw were recorded using the RC Benchmark software. Using equation 1, the recorded airspeeds at 0 m/s freestream velocity were compared to the thrust measurements from Phase 1 and were within 8%, ensuring reliability. Using the recorded thrust measurements from Phase 2 at the five tested airspeeds, a propeller efficiency relationship was developed to inform the simulation. This efficiency relationship is shown in Figure 5.4 below, with efficiency decreasing linearly as the freestream velocity increases.

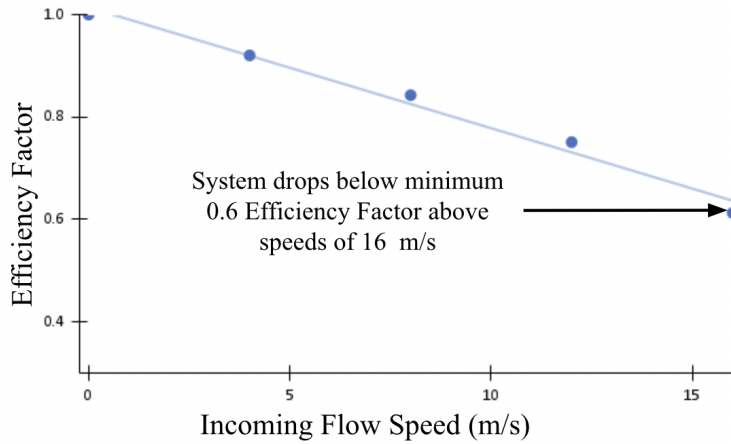


Figure 5.4: Propeller Efficiency

Our testing confirmed that at flow speeds greater than 15 m/s, the propeller efficiency drops off enough that the propeller would be unable to accelerate flow quickly. Thus, the Phase 2 testing validated our decision to limit the cruise speed of the simulated aircraft to 15 m/s.

### 5.3 Phase 3 - Wing Aerodynamic Performance Testing

To validate the results of the simulations of the performance of our chosen airfoil, we tested the aerodynamic performance of the constructed wing in the 5 ft-by-7 ft wind tunnel. A photograph of the test setup is shown in Figure 5.5 below.

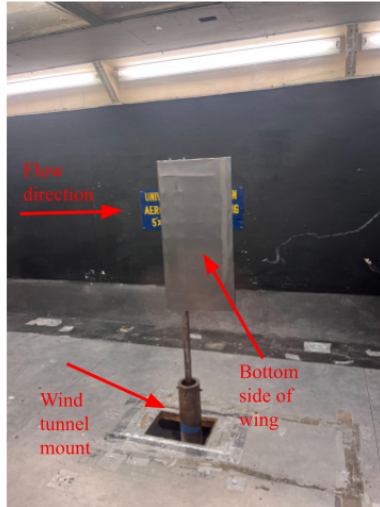


Figure 5.5: Wing Performance Test Setup

Wing performance was characterized by conducting tests across the entire stall profile of the wing at incoming flow speeds of 5 m/s, 10 m/s, 15 m/s, and 20 m/s. Prior to the start of testing, we calibrated the load transducers of the tunnel using the standard data acquisition system (DAS) procedure. This procedure involves placing known weights onto the load transducers connected to the DAS and verifying the computer displays correct force values. and verified that the force readings were accurate under a known load. Each stall profile characterization used  $\pm 2^\circ$  angle of attack ( $\alpha$ ) increments near  $0^\circ$  and changed to  $\pm 1^\circ$  increments as the wing approached a stall. Multiple data points were taken using the DAS at each angle of attack to study hysteresis. Additionally, we ran tests with just the spar mount in the tunnel to properly characterize the drag it was responsible for.

Using the results of the wing performance test, we generated plots of lift coefficient ( $C_L$ ), drag coefficient ( $C_D$ ), and pitching moment coefficient ( $C_M$ ) with respect to the wing's angle of attack. Each data point includes an error bar to characterize any differences between data points at that particular angle of attack. The plots are given below in Figures 5.6, 5.7, and 5.8 (see Appendix F for plot raw data).

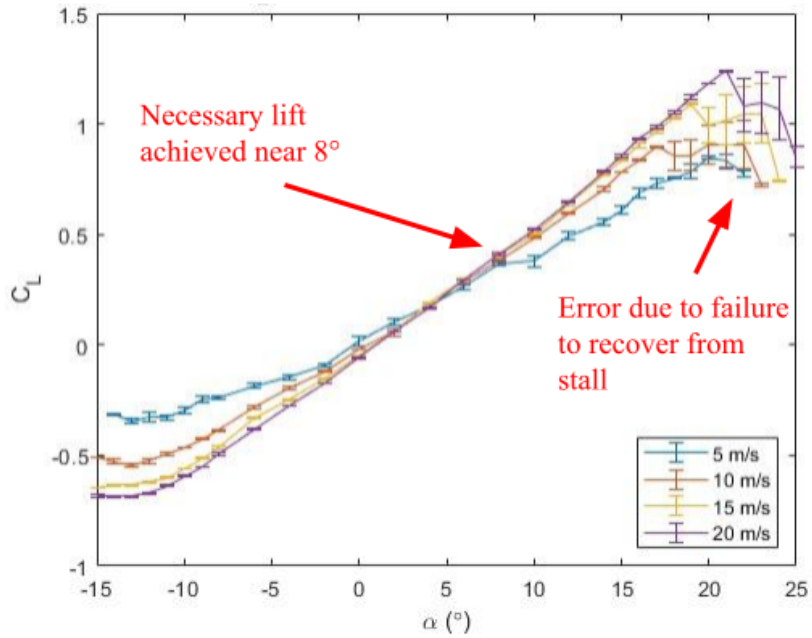


Figure 5.6: Wing Lift Characterization

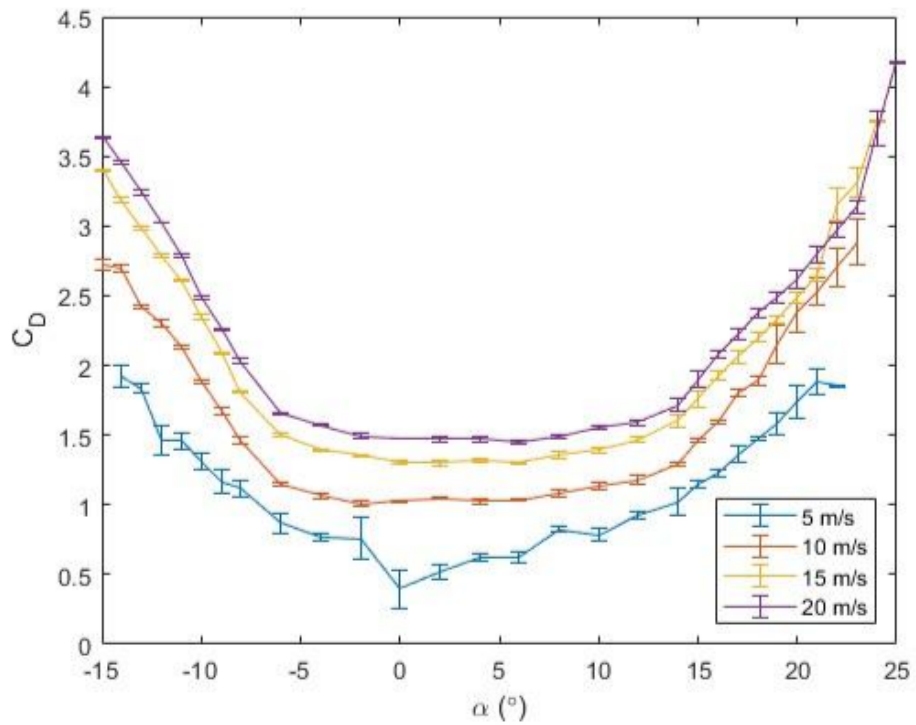


Figure 5.7: Wing Drag Characterization



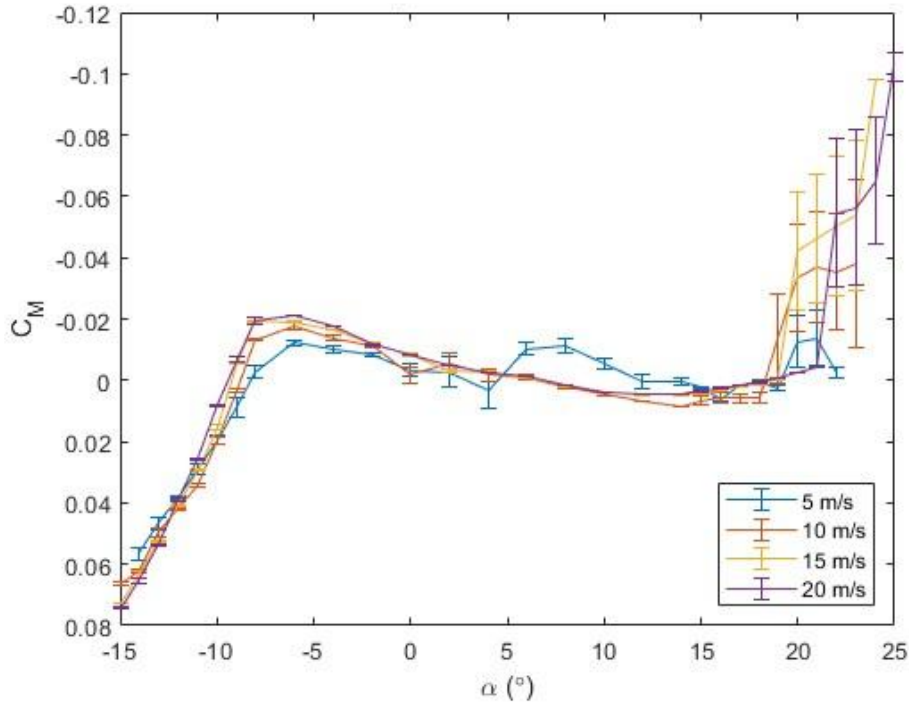


Figure 5.8: Wing Pitching Moment Characterization

One important simplification for this test is that we did not correct for blockage. Since the wing is mounted vertically in the wind tunnel, the characteristic cross section is roughly  $0.0367 \text{ m}^2$ , while the 5 ft-by-7 ft wind tunnel has a cross sectional area of  $3.25 \text{ m}^2$ . This results in a blockage ratio of approximately 1%. According to most references, no corrections for blockages are required when the blockage ratio is less than 3% [1]. Thus, we did not correct for blockage effect since it would not have a significant impact on our final results.

In comparing our testing data with our simulations, we found that our wing section did not have the same performance as predicted by the simulation. At cruise speed, our simulation predicted that our wing would generate the required lift at  $4^\circ$  angle of attack. During our testing, we found that our wing generated that same lift at  $8^\circ$  angle of attack. We believe that the discrepancies between the simulated performance and actual performance are due to the limitations of the simulation program, as well as manufacturing defects of the wing. More details on the simulation can be found in Appendix G. The differences found between the simulation performance and actual performance were analyzed and included in the full aircraft simulation. Nevertheless, our wing section met its requirement of generating 7 N of lift.

#### 5.4 Tilt Mechanism Functionality Testing

Before we tested our tilting mechanism in the wind tunnel, a static test was performed to ensure that the software would still actuate the servo in the desired  $3^\circ$  increments. The test was performed by placing the servo on its side in front of a sheet of paper and actuating it across the testing range of  $0^\circ$  to  $90^\circ$ . Each increment was achieved once, starting with the minimum and maximum and increasing or decreasing by  $3^\circ$  until finding the middle of the range at  $45^\circ$ , all while marking each point with a pencil. By conducting

the test in this way, we were able to capture the effects of the largest possible actuations as well as the smallest. Following the completion of the test, each angle was measured using a protractor and compared to the intended angle. We determined that each desired angle at 3° increments is accurate to within 1°, with most of the difference being due to human error during the protractor measuring process. Therefore, our servo actuation requirement was met.

In addition to static testing, we performed tests with the servo under load to verify that any aerodynamic loads in the wind tunnel would not impact the tilt mechanism's performance. A photograph of this test is given below in Figure 5.9.



Figure 5.9: Tilt Mechanism Load Test Setup

By hanging a bag with 3.5 pounds (lbs) of weight from the tilt mechanism and rotating the servo throughout its range of motion, we were able to observe that neither servo performance nor structural integrity of the mount were affected. Based on this, we believe that our test article is successful in meeting the structural reliability requirements.

## 6. Simulation

To allow our team to quickly simulate and explore different servo tilt profiles without having to manually test each individual one, we created a Simulink model to replicate the conditions and forces during a VTOL drone's transition. This model is based on our PM's drone and incorporates data from the previous component characterization tests for our team's propulsion system and wing section. The model considers the dynamic efficiency loss of the propeller, the wing's aerodynamic properties, and the propeller's thrust-to-power correlation. At a high level, this model takes in time dependent arrays of servo tilt angles that are then simulated to determine the corresponding thrust output, power consumption, and altitude change. A more detailed explanation of this model is provided in Section 6.1, and the results of the simulation are then discussed in Section 6.2.

## 6.1 Model Overview

The Simulink model consists of three main components: the servo tilt profile input, the thrust controller, and the plant. Each of these components can be seen in Figure 6.1 which shows the complete Simulink model.

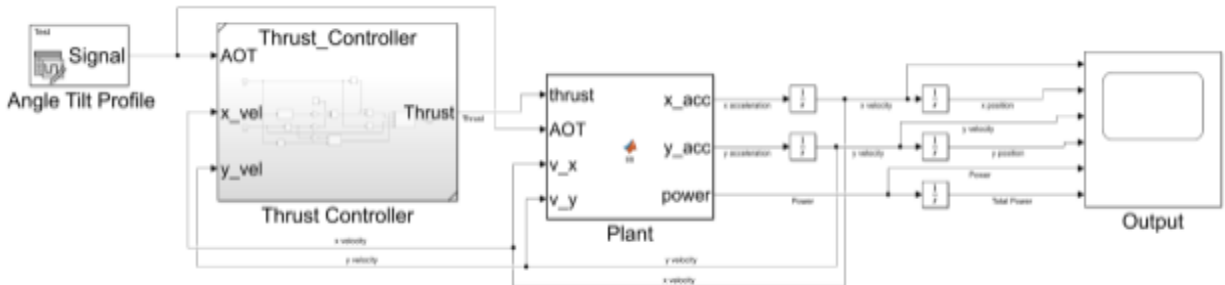


Figure 6.1: VTOL Drone Transition Simulink Model

Beginning with the servo tilt profile, this is a signal input that relates the servo angle, and thus propeller angle, to time. Like the transition profiles discussed in Section 1.1, these tilt profiles have a  $90^\circ$  tilt angle corresponding with an upward vertical motor orientation and  $0^\circ$  angle corresponding with a forward horizontal motor configuration. Figure 6.2 below shows an example of a linear servo tilt profile in Simulink's Signal Builder. The first 2 seconds of this signal corresponds with vertical flight which is then followed by an 8 second transition period and concludes with a 2 second cruise period.

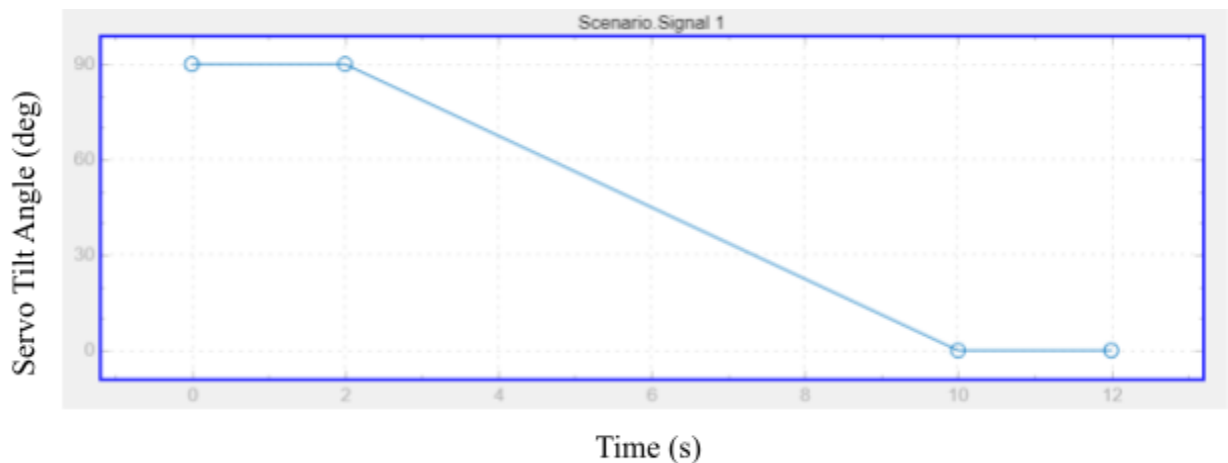


Figure 6.2: Example Simulink Servo Tilt Profile

These tilt profiles are then fed into the next major component of the model which is the thrust controller. The thrust controller takes in the current tilt angle and the aircraft velocity and computes the necessary thrust required for the drone to maintain constant altitude. This is done using Newton's laws of motion in the vertical direction. There are four forces in the vertical direction that can all be computed: wing lift, vertical drag, weight, and propeller thrust. The lift generated from the wing is estimated using data from the wing characterization test and the current horizontal velocity, the vertical drag is computed using a rectangular coefficient of drag estimate and the vertical velocity, and the weight of the drone is known

from the PM's requirements. This then only leaves the vertical component of propeller thrust which can then be computed to balance out the rest of the forces and maintain constant altitude. Once the necessary propeller thrust is known, the thrust, tilt angle, horizontal velocity, and vertical velocity are fed into the plant which includes the drone's state space model. This state space again uses Newton's laws of motion to compute the forces in the horizontal and vertical direction. Once doing so, the forces can be integrated out to get velocity and position, which are then fed back into the next iteration. Additionally, the plant also computes the necessary power for the motor based on the dynamic propeller testing conducted earlier in the study. The model outputs plots of the drones position, velocity, thrust, and power curves as a function of time. The transition profile relating power as a function of tilt angle can also be output. For a more detailed view of the state space refer to Appendix H.

## **6.2 Simulation Results**

The simulation was used to analyze not only the transition profile's shape but also the profile time duration. This section of the report is broken down into two sections, with the first section analyzing different profile shapes and the subsequent analyzing the profile duration.

### 6.2.1 Transition Profile Shape

In order to gain insight into the power consumption of our PM's drone during its transition phase, we began by testing tilt profiles using standard functions to observe how the drone would respond to different profile shapes. We tested linear, cosine, exponential, negative quadratic, and positive quadratic profiles and assessed their impact on the drone's behavior. There are an infinite number of possible tilt profile functions, such as step functions and changing slope functions, but they were not any more useful in describing the observed phenomena. The tilt profiles included below are for brevity and clarity. To read more about these additional profiles, please refer to Appendix I and Appendix J. Nevertheless, by exploring a range of functions, we developed a deeper understanding of how the drone's power consumption would respond to any general profile shape. The previously mentioned transition profiles can be seen below in Figure 6.3 which shows the tilt angle as a function of time as well. All of these transitions consisted of a 2 second vertical takeoff followed by an 8 second transition and a 2 second cruise period. By maintaining a constant transition duration, this section is able to investigate how different profile shapes affect power consumption independent of time. The transition power consumption and its relation to time is analyzed in the following section.

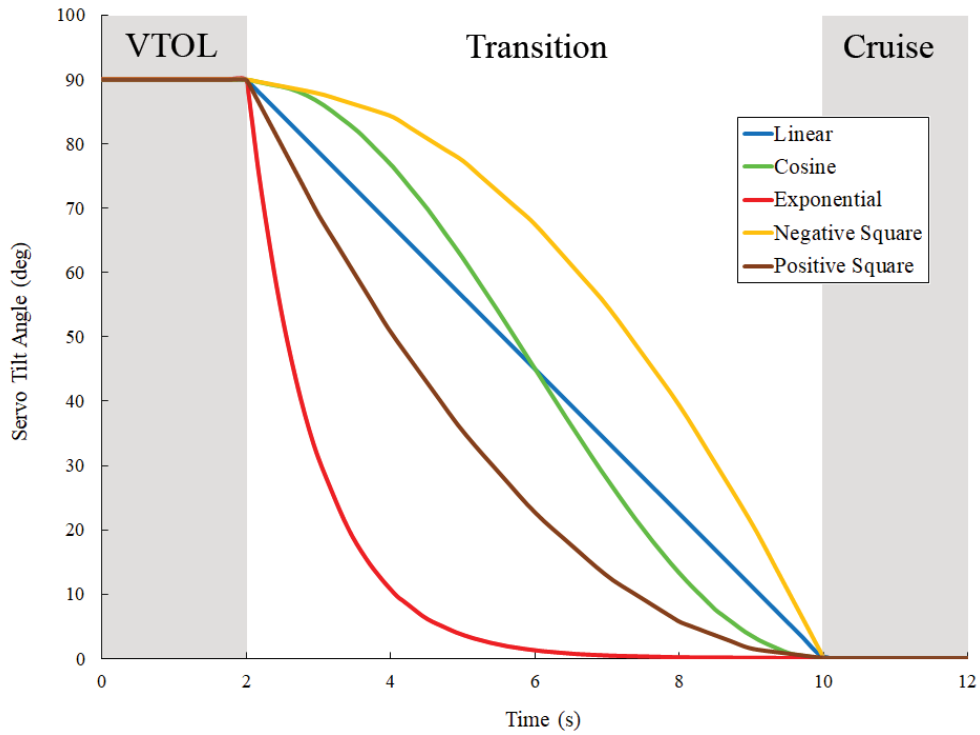


Figure 6.3: Simulated Transition Profile Functions

Each of these transition profiles corresponds with a unique power consumption profile. These power consumption profiles, which relate motor power to time, are shown below in Figure 6.4.

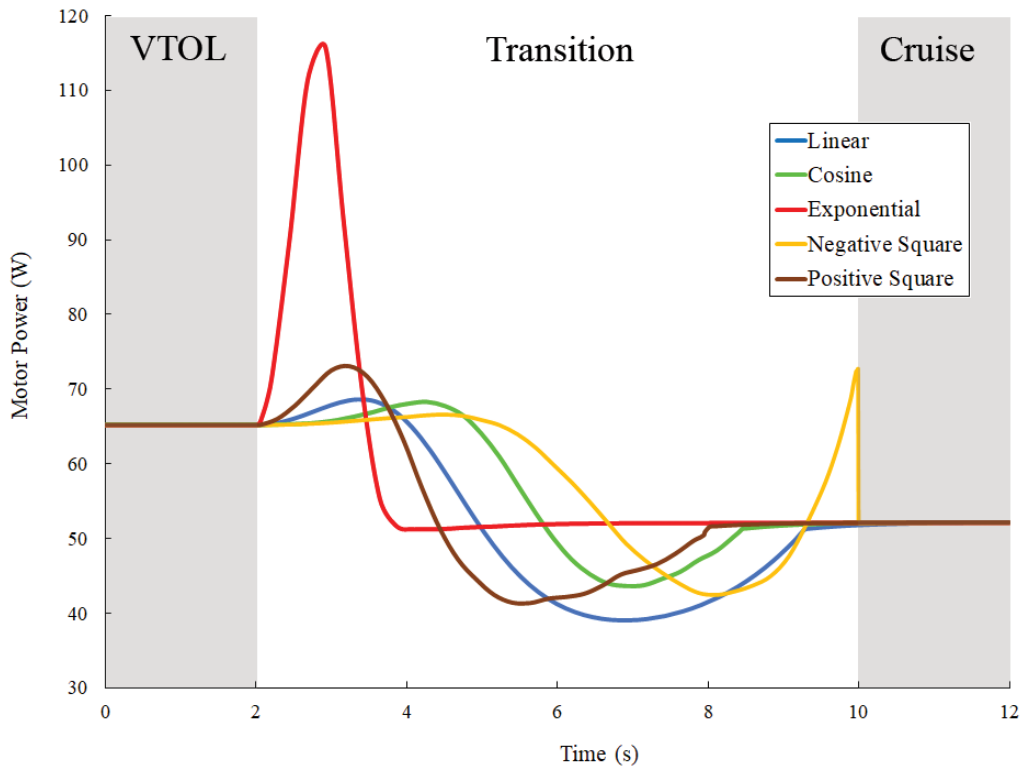


Figure 6.4: Power Consumption for Simulated Transition Profiles

The corresponding power consumption profiles for the different functions vary greatly. Most importantly, each profile has a different peak power consumption differing all the way from 68 W to 115 W. Some profiles even have two power peaks such as the negative square function. These peaks can all be explained by analyzing the drone's states throughout its transition. At the beginning of the transition, the power increase is due to the drone losing vertical lift by tilting the motor downward and not being able to gain much lift from the wing due to the low horizontal velocity. Moreover, the varying peak amplitude is due to the initial slope of the tilt profile. For example, the exponential function has a steep initial slope and therefore the drone loses the vertical force component quite quickly which causes a steep increase in motor power to maintain constant altitude. Conversely, the negative square function has the smallest initial slope which then results in the smallest initial peak amplitude.

Once the drone builds up horizontal velocity, the lift from the wing increases and the motor power is able to decrease from its peak. This continues until the drone reaches its minimum power consumption which is slightly lower than the cruise power consumption. This is because at the minimum power consumption the drone's tilt is at roughly 25-40° which means it still has a lift contribution from the propeller and from the wing. However, it is not ideal to cruise in this low power consumption if covering distance is the mission goal as the drone is still going quite slow. After reaching the minimum power point, the drone then has to increase its thrust at the end of its transition to reach its cruise thrust. This can result in a second peak which can be seen in the negative square profile. This profile creates this second peak because the slope near the end of the transition is too high. This results in the drone not building up enough horizontal velocity throughout the transition and having to greatly speed up near the end to reach

its cruise velocity, therefore resulting in a second power spike. When the exponential and cosine functions are reflected about the linear profile, they produce profiles with a similar, but more pronounced, second power peak as well and thus were not included in the analysis.

Interestingly, even with the wide range of peak power amplitudes, the overall power consumption of the transitions are relatively close. Table 6.1 below shows the peak power and total power consumption for each of the profiles. The linear profile has the minimum total power consumption and the cosine profile has the minimum peak power. The negative square profile does have a smaller initial peak power than the cosine profile, but its second peak actually increases above its initial peak.

Table 6.1: Peak and Total Power Consumption for Simulated Transition Profiles

<b>Transition Profile</b>	<b>Linear</b>	<b>Cosine</b>	<b>Exponential</b>	<b>Negative Square</b>	<b>Positive Square</b>
<b>Max Power Peak (W)</b>	68.6	68.3	115.8	72.7	73.1
<b>Total Power Consumption (J)</b>	406.4	449.0	474.5	456.7	426.2

Based on the results, it can be concluded that the linear profile is the most optimal choice for power consumption, as it consumes the least amount of total power and has the second lowest peak power. Specifically, the peak power of the linear profile is less than 0.5% higher than the cosine profile, which has the lowest peak power among all the profiles tested. Therefore, the linear profile is the best option as it not only reduces the total power consumption, but also keeps the peak power under control. Moreover, the linear profile would be more stable than many of the other profiles as there are no steep power changes. To see all of the drone’s states (position, velocity, etc.) during the linear profile’s transition, please refer to Appendix K.

### 6.2.2 Transition Profile Duration

After determining the linear profile is most ideal, another study was conducted to analyze the ideal duration of the transition. This was done by simulating multiple linear profiles varying in duration from 4 seconds to 12 seconds in 2 second intervals. The resulting power consumption profiles for the multiple linear profiles can be seen below in Figure 6.5.

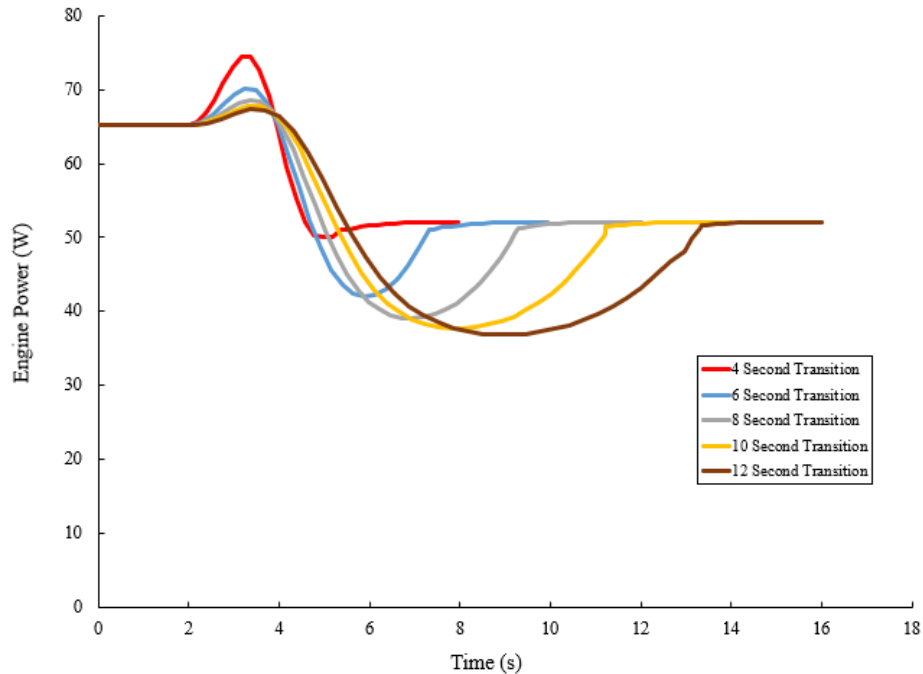


Figure 6.5: Power Consumption of Varying Duration Linear Transitions

It can be seen in the graph above that as the transition time decreases, the overall peak power decreases as well. This matches the intuition in Section 6.2.1. which indicated that the initial tilt slope corresponds with the amplitude of the peak power. Moreover, the minimum power decreases as the transition duration increases. This is because in shorter transitions the drone does not have as much time to build up horizontal velocity and benefit from the combined wing and propeller lift at low tilt angles. Moreover, there is a linear relationship between overall power consumption and transition duration. As the transition duration increases, so does the total power consumption. This makes sense because the drone stays in the air longer for longer transitions and thus would consume more power. In addition, longer transitions cover a greater distance, but this is not particularly useful as covering distance is better achieved during cruise rather than transition. These relationships can be seen in Figure 6.6 below which shows how both the maximum peak power and the overall power consumption is related to the transition duration.



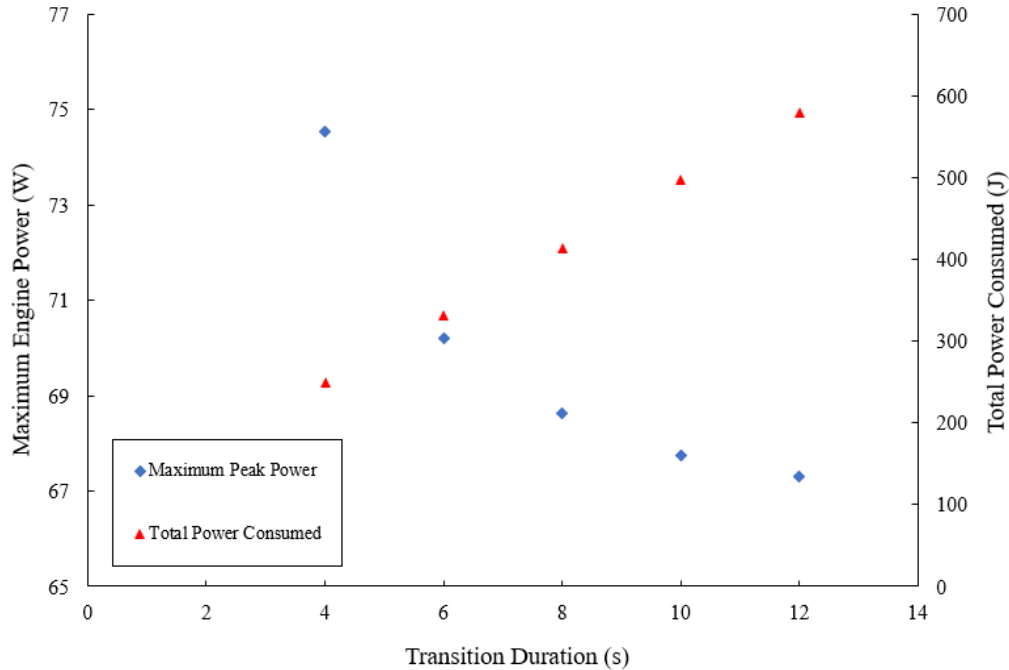


Figure 6.6: Peak and Total Power Consumption of Varying Duration Linear Transitions

Therefore, it can be seen that in order to decrease the total power consumption as much as possible, the transition duration should be minimized as much as possible until the peak power consumption aligns with the maximum possible engine power.

## 7. Simulation Validation Testing

In order to validate the accuracy of our simulation, our team tested the fully integrated tilt rotor test article in the University of Michigan 5 ft-by-7 ft wind tunnel. Unfortunately, due to time constraints, we were only able to perform validation testing for the linear tilt profile. The procedure and results of this test are detailed in this section.

### 7.1 Test Procedure

The first step was to calibrate the wind tunnel load transducers using the standard procedure for the DAS detailed in section 5.3. After calibration, we verified that a known load produced the expected DAS output. Next, we placed the tilt rotor wing test article into the wind tunnel. We set the angle of incidence of the wing to be  $9^\circ$ . This was determined to be the required angle for the goal lift of 5N at cruise using results from our wing aerodynamic performance testing (Section 5.3). Once the test article was in place, the tilt rotor mechanism was iterated through its full range of motion from  $90^\circ$  to  $0^\circ$  relative to the free stream. This was mostly a sanity check of our command inputs, since those had to account for the angle of incidence. Lastly, we ensured full throttle control of the motor using a DC power supply set to 16.8 V (equivalent to a full 4S LiPo battery). We decided to use a DC power supply instead of a battery to mitigate the risk of battery issues and the effect of low charge, and it was set to a 4S equivalent since a 3S equivalent setting would not stay in the ‘Constant Voltage’ operational mode. Once complete, we were ready to turn on the tunnel.

From our simulation, we had arrays of tilt angle, horizontal velocity, and motor power. Our procedure was to accelerate the tunnel to a known velocity and tilt the motor to the associated angle before powering the motor. Then, when ready to collect data, we would activate the motor and ensure that the lift from the propeller and wing combined produced the required 5N of lift. This emulates the aircraft maintaining altitude as well as the forward motion of the aircraft. The power consumption read on our power supply was recorded.

One potential source of error is the energy added to the flow by the propeller, but this was mitigated by turning off the propeller and allowing the tunnel to stabilize at the desired airspeed before each data point. The following section details the results of our testing.

## 7.2 Test Results

Figure 7.1 shows both the simulated and tested transition profiles for a linear tilt profile input. It is evident that while the simulation may underestimate at high tilt angles and overestimate at low tilt angles, the general behavior of the power consumption is well modeled by the simulation.

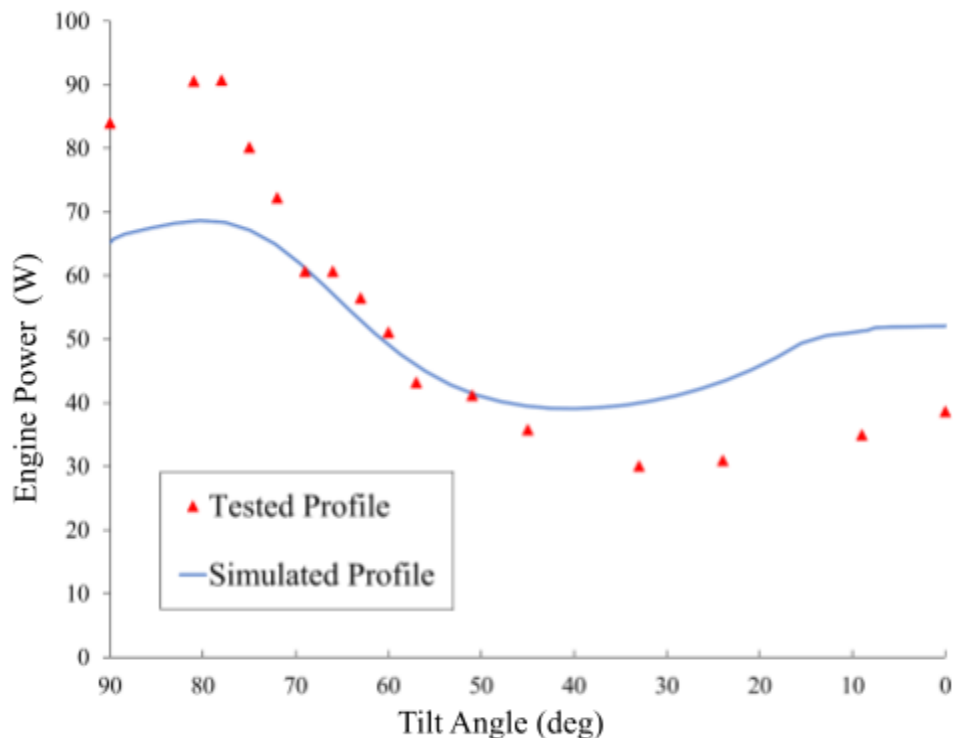


Figure 7.1: Simulated and Tested Transition Profiles for Linear Tilt Input

The test data shows that the peak power for a linear transition is 92 W, which is 30% higher than what was predicted during the simulation. The test data also shows that the full aircraft simulation overestimates the power requirements as the aircraft approaches horizontal flight. Discrepancies between the simulation and testing could be caused by a variety of factors. One cause could be efficiency losses

during energy transmission to the motor due to long wires and excessive connections. Another could be that the wind tunnel test cannot perfectly be used to replicate a flight test. Or perhaps the test article fabrication could be improved. Nevertheless, the aircraft simulation was validated by the test data as the collected data follows the expected trends and values. Further actions would be to characterize and mitigate the aforementioned sources of error and to improve the fidelity of the simulation.

## 8. Project Schedule and Budget

This project was intended to be completed within a 16-week schedule with a test article construction budget of \$500.00 USD. Below, Figure 9.1 shows our project Gantt chart that compares our proposed schedule with our actual schedule.

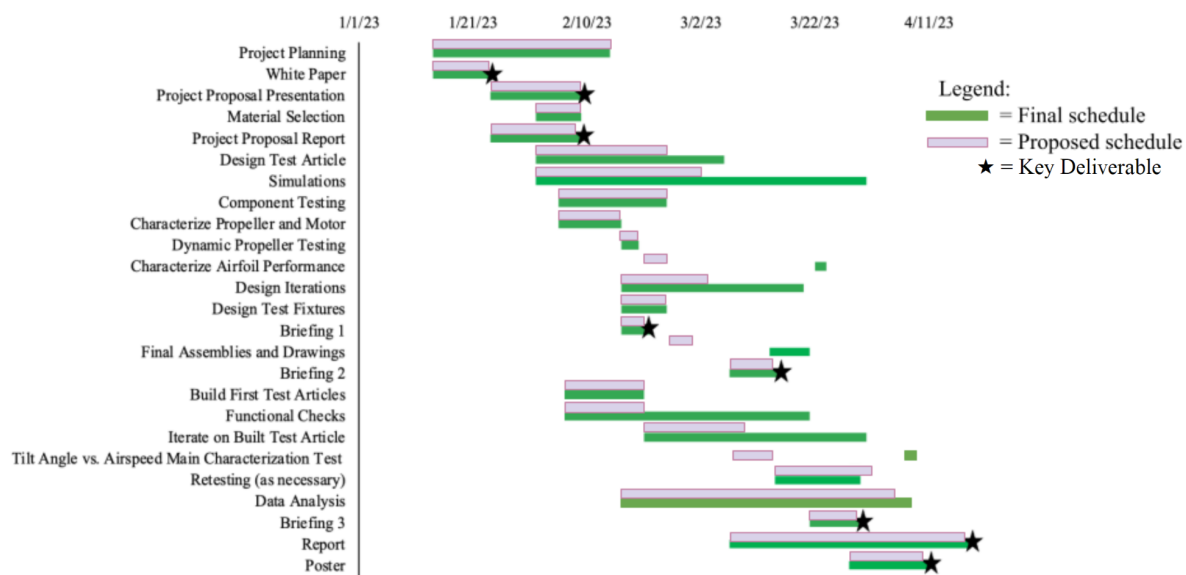


Figure 8.1: Project Gantt Chart

Our project underwent several delays, but we were able to complete our task on time since we added margins for re-testing. The most significant delays were due to difficulties in manufacturing the wing test article and due to component malfunctions during the Tilt Angle vs. Airspeed Main Characterization Test (Validation Testing). Despite setbacks, we were able to complete our project on-time and produce our final deliverables with time to spare.

In order to ensure that work was progressing steadily and that we were prepared to meet our required deadlines, we recorded the number of hours spent working on the project. Figure 9.2 shows the total team work hours as a function of ‘semester quarters’. The semester quarters were roughly delineated by our three progress briefings and this final report.

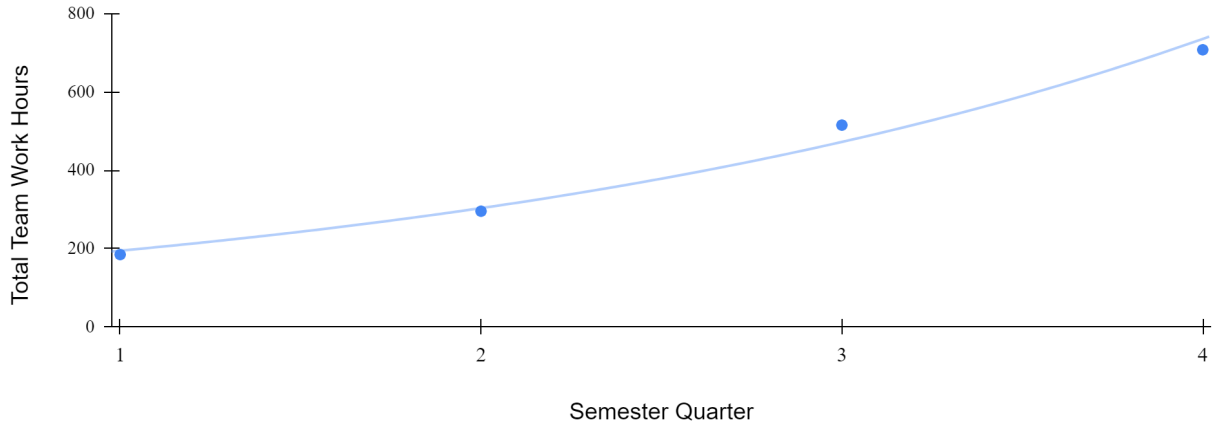


Figure 8.2: Cumulative Hours Spent on Project

As you can see, the total team work hours increases exponentially as the semester progresses. This was expected since the team experienced delays due to manufacturing and technological difficulties. In order to stay on schedule and produce substantial results, an acceleration of workload was required. In the end, the team managed to produce tangible results, but of course there is always more work to be done.

In total, this project cost \$86,412.98 with the majority of the expenses due to labor costs. The final costs are higher due to the proposed costs of \$54,640.00 because of higher than anticipated hours worked, and facilities usage. However, labor and facilities were provided by the University of Michigan and their cost did not impact the team. We were limited to \$500.00 for the construction of the test article, and we spent a total of \$272.98 on electronics, hardware, and materials which is well under our maximum budget. A breakdown of proposed vs. actual costs are shown in Table 9.1. For a full itemized list, see Appendix L.

Table 8.1: Simplified Proposed vs. Final Budget Breakdown

Category	Item	Proposed Cost	Actual Cost
<b>Labor</b>	Engineer	\$48,000.00	\$84,840.00
	Consultant	\$500.00	\$500.00
<b>Facilities</b>	Shop	\$400.00	\$500.00
	Wind Tunnel	\$360.00	\$300.00
<b>Test Article</b>	Electronics	\$220.00	\$39.52
	Hardware	\$65.00	\$137.43
	Materials	\$95.00	\$96.03
<b>Contingency</b>	.	\$5,000.00	-
<b>Grand Total</b>		\$54,640.00	<b>\$86,412.98</b>

## 9. Conclusions and Recommendations

No single tilt-profile is able to succeed in all criteria of optimizing both peak power requirement and total energy consumption during transition. While holding transition time constant, we found that a linear transition profile minimizes total energy consumption, while a cosine transition profile minimizes the peak power requirement. Despite this, the differences in peak power between a linear transition profile and a cosine transition profile are quite small, and therefore we recommend that the PM's small bi-rotor tilt rotor drone utilizes a linear transition profile.

Secondary investigations show that there is an optimal transition time for tiltrotor drones depending on weight and propulsion configurations. Our studies show that there is an inverse relationship between peak power requirement and total energy consumption as transition time changes. For very short transitions, the peak power requirement drives system design but for very long transitions, the total energy consumption is the main driver. For the PM's small bi-rotor drone, we recommend a 6 second transition time as this is the duration where the maximum peak power required aligns with the drone's maximum available power.

For the continuance of this project, we would highly recommend validation testing of more tilt profile shapes, namely the cosine transition and the positive square transition profiles. To add more realism into the validation testing, we recommend automating the tilt-profile using airspeed and acceleration sensors which would provide more real-life data into the performance of the tiltrotor. Finally, we recommend updating the test articles with a more conformed wing and a redesigned motor mount that has better functionality and less potential interference with the propeller airflow.

## Appendix A - Project Manager Nicholas Mellanby's Prototype Tilt Rotor Drone

M-Tilt Project Manager, Nicholas Mellanby, created a prototype tilt rotor drone for his Engineering Honors Program capstone project. The requirements of this drone directly influenced those of the general study. This appendix will outline those requirements, the design, and the construction of the drone, as well as challenges faced in the process and future improvements.

### A.1 Requirements

The drone was required to have a weight of 10 N (1.01 kg) and a thrust-to-weight ratio of 1.4, a value consistent with aircraft of this type [3]. The aircraft was required to cruise at or above 15 m/s, and the configuration was required to be a bi-rotor with wingtip mounted propellers capable of tilting.

### A.2 Wing Design

Using Solidworks, a popular CAD software, the prototype design was created. An isometric view of the prototype CAD is shown below in Figure A.1.

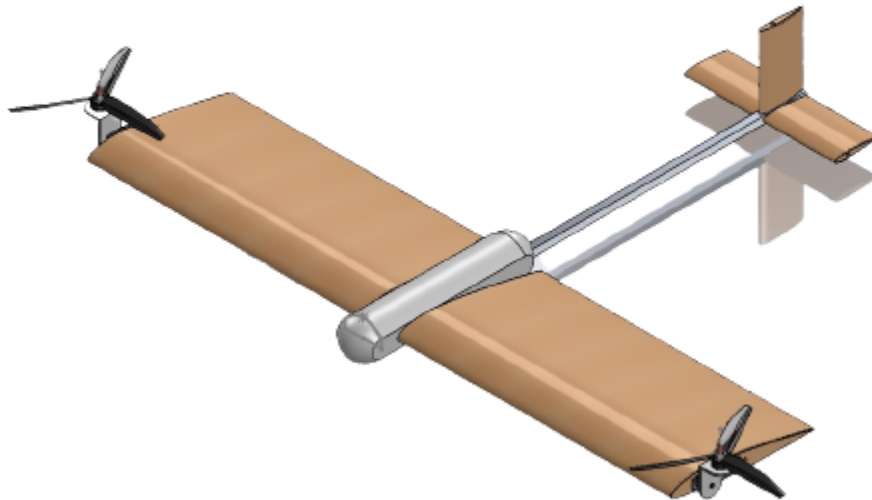


Figure A.1: Isometric View of Tilt Rotor Drone Prototype Assembly

As you can see, the design configuration is a bi-rotor with wingtip mounted tilt rotors. The fuselage is a 3D printed cylinder that can house a BeagleBone Blue flight controller and a 3S-4S LiPo battery. The ESCs, wiring, and servos were all designed to be located within the wing. Based on the requirements and an airfoil thickness of 1.2 in. to accommodate these electronics, the airfoil was selected to be a NACA 24012. Figure A.2 shows the general rib design. Other variants of this rib design were used in certain locations, such as at the servo mount, but they do not differ enough to include in a separate image.



Figure A.2: NACA 24012 Airfoil with Spaces for Support Structure and Electronics

Figure A.2 also shows that the wing is designed to have two support spars, evidenced by the two quarter-inch diameter holes. The wings are two 19-in. span sections each with a chord length of 10 in., giving an aspect ratio of 3.8. Furthermore, the wing's incidence angle is set at  $5^\circ$  based on historical data [3] and preliminary calculations which determined sufficient lift was produced at this angle of attack and the required cruise speed.

During the design process, the center of gravity deliberately was maintained at roughly one inch aft of the wing quarter chord point for two reasons. One, based on topics discussed in the class Aerospace Engineering 481: Aircraft Design, the center of gravity should be as close to the quarter chord as possible for in-flight stability. Two, the center of gravity should be as close to in line with the center of thrust as possible in VTOL aircraft for hover stability. Since the propulsion system is mounted just aft of the quarter chord in the design, this is where the center of gravity should be too.

It is worth noting two changes to the design shown in Figure A.1. The first is the use of a torque bar tilting mechanism rather than one that is wingtip mounted. Upon consulting Professor Thomas Miller on the wingtip tilting mechanism, there was concern about potential instability and bending caused by the propulsion system and other aerodynamic forces. A torque bar alleviates these issues by mounting the propeller to a rotating rod supported by a pillow block bearing and the existing wing support structure. This pillow block and support structure handle the bending loads, while the rod (in this case of carbon fiber) handles the torque created by aerodynamic forces during tilting. This significantly reduces the loads on the servo. Figure A.3 shows this mechanism in the prototype. The second major change is the use of a flat plate tail rather than one with an airfoil cross section. Many hobbyists use simple flat plates in place of horizontal and vertical stabilizers, since they are simple, light, and equally as effective at low airspeeds. This drone employed this design choice for those very reasons.

### A.3 Construction

Construction began with a 48- by 0.5- by 0.25-in. aluminum wing spar and a 29.5- by 0.5- by 0.5-in. aluminum body spar already available in the Aerospace 405 Lab. The spars were assembled in a T-shape with the 3D printed fuselage attached at the same time. The fuselage was fused around the spars using cyanoacrylate glue.

Next, the ribs were laser cut from 1/16-in. balsa wood. Thirteen ribs were used per wing section, giving twenty-six total. The ribs were adhered to the main spar and the support spars using cyanoacrylate glue once again. The ribs were generally placed at a spacing of 1.75 in., deviating to accommodate the tilting mechanism. This can be seen in Figure A.3 below.

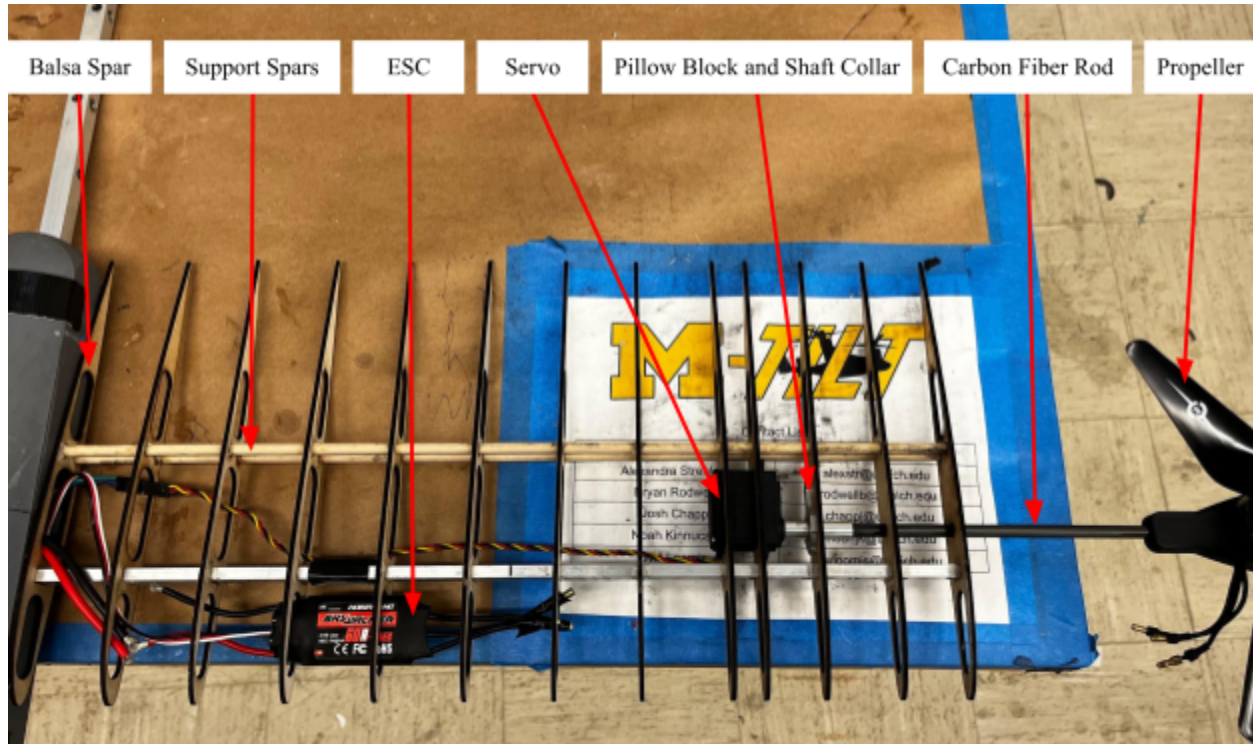


Figure A.3: Wing Structure and Tilting Mechanism

The tilting mechanism consists of a HiTec HS-5645MG 10 kg-cm servo, an aluminum shaft collar, an aluminum pillow block with a bearing, and a 7 millimeter (mm) diameter carbon fiber rod. The shaft collar and pillow block bearing came as a pair, so they fit perfectly together. With a 7 mm interior diameter on the shaft collar the carbon fiber rod also fits perfectly. The motor and propeller were then mounted to the carbon fiber rod via a 3D printed mount. The functionality of this tilting mechanism is excellent, exhibiting smooth rotation, responsiveness, and a range of motion beyond that necessary to both hover and cruise.

Once the wiring was finalized and confirmed to be functional, the wing was covered in Monokote. The wing was first covered with 1/64th in. balsa wood on the leading and trailing edges as well as at the wing tip and wing root. This was done so that the Monokote covering had a surface to adhere to. Figure A.4 shows one wing covered in Monokote and one wing with just the balsa surfaces. More details on the Monokoting process can be found in Appendix B.





Figure A.4: Prototype Drone During Wing Monokoting

Lastly, the flat plate tail was attached to the rear of the body spar. These surfaces were also Monokoted to provide a smooth surface for airflow to interact with. The completed prototype is shown in Figure A.5 below at the University of Michigan Design Expo.



Figure A.5: Full Prototype on Display at The University of Michigan Design Expo

Fully constructed, the drone has a weight of 17.36 N and a thrust-to-weight ratio of 1.325. The thrust-to-weight ratio was achieved by using the propulsion configuration from Section 4.2 with a 4S LiPo, garnering 11.5 N of thrust from one propeller (23 N in the bi-rotor configuration). Unfortunately, however, the drone was not flight tested. The following section discusses challenges faced in getting the aircraft flight worthy.

#### A.4 Challenges Faced

The first major challenge was weight inflation. While a CAD estimate can give a solid preliminary idea of the vehicle weight, it is not perfect. Even accounting for a 10% margin of growth, the final weight ended up 73% heavier than the required 10 N. That said, utilizing a 4S battery with a weight only 36g heavier than its 3S predecessor enabled a thrust-to-weight ratio that was quite close to the goal. In theory, this vehicle could easily get off the ground.

The true issue that prevented a flight test was software. As mentioned earlier in this appendix, the flight controller was an off-the-shelf product known as a BeagleBone Blue board. These boards are compatible with an open source flight software called ArduPilot. ArduPilot has code bases for all types of aircraft, including bi-rotor drones. The plan for this prototype was to save time by utilizing this open source software, modifying it to leverage the tilting mechanisms for roll and vectored thrust for yaw. However,

the board had a major issue that prevented it from functioning properly even after the set up procedures were followed with completely successful indicators along the way. Due to time and budget constraints, developing the control algorithms in house or acquiring a new flight controller were not realistic; moreover, issues encountered by the M-Tilt team took precedence as deadlines approached.

#### A.5 Conclusions and Future Work

In conclusion, the prototype drone developed by Project Manager Nicholas Mellanby demonstrates the complexities of designing tilt rotor drones, let alone flying them. However, an extremely successful prototype was created in terms of structure, especially in regards to the tilting mechanism. With regards to transition flight, the requirements of this drone drove the M-Tilt study of the transition between vertical and horizontal flight in tilt rotor drones to increase efficiency of power consumption. From that study, meaningful results were produced. Future work will focus on the construction of a second prototype. Lighter materials such as carbon fiber will be leveraged for the spars and the fuselage, and the flight controller will either be debugged or replaced.

## Appendix B - Wing Section Manufacturing Methods

Constructing a conformed wing section test article posed a challenge during this project. Since our test article was supposed to be representative of a flying vehicle, it was imperative that the built wing conformed to the dimensional specifications of our proposed design. At first, we intended to build our wing using a sandwich composite structure with a foam core and resin-reinforced fiberglass as the face sheets. We believed that a composite wing would provide us with the most uniform wing shape and would also have a smooth leading edge and upper surface which is extremely important for aerodynamic performance. We used *Composite Construction for Beginners* as our main reference during composite construction [6].

During construction of our first wing section prototype, we ran into troubles with tooling. We had intended to use a computer numerical control (CNC) foam cutter to cut our airfoil sections, but we quickly discovered that the equipment was inoperative. This left us with a manual hot-wire foam cutter, which was functional but subject to human error in both setup and operation. In using the manual foam cutter, we found it difficult to cut conformed airfoil sections despite use of a balsa rib template. We also experienced issues during the lay-up process. The flox filler we intended to use to fill gaps did not mix well and became a paste that made processing difficult. Without the flox, we experienced delamination of the face sheets from the foam core. Despite our efforts, we were unable to produce a conformed wing section using the composite materials (Figure B.1). Since building another composite wing section has a significant lead time, we opted to switch to a wood and MonoKote wing structure which takes less than one day to manufacture.

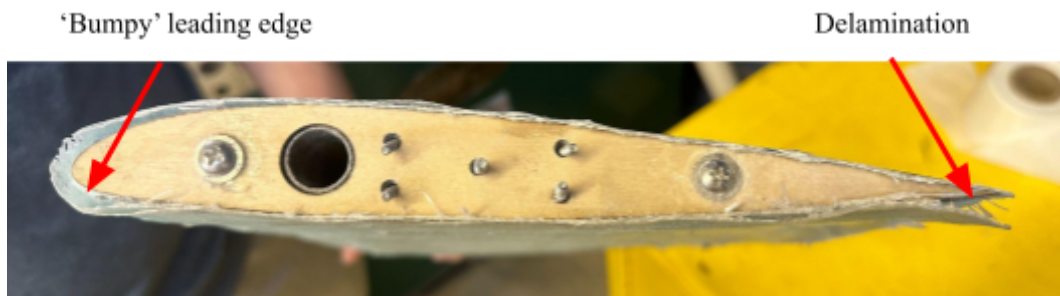


Figure B.1: Prototype Composite Wing Section

The MonoKote wing proved easier to manufacture than the composite wing, but it also had its own limitations. Since MonoKote is a plastic sheet with heat-activated adhesive, it essentially shrink-wraps to the structure that it is applied to. Thus, MonoKote is prone to webbing. As seen below in Figure B.2, the webbing prevents a smooth upper surface due to the rib edges protruding slightly through the skin.



Figure B.2: Webbing Effect on MonoKote Wing

To mitigate the webbing issue, we used 1/32 in. balsa sheets on the leading edge, trailing edge, and sides of the wing section. The secondary benefit of using these formed balsa sheets was that they provided a larger surface for the MonoKote to tack to. To create the curve of the leading edge, the balsa sheets were wetted with ammonia and water (Windex) and then molded around the ribs. The balsa was held in place as it dried, and then was glued on using cyanoacrylate (CA) glue. The location of the balsa sheets are shown as red rectangles in Figure B.3 below.

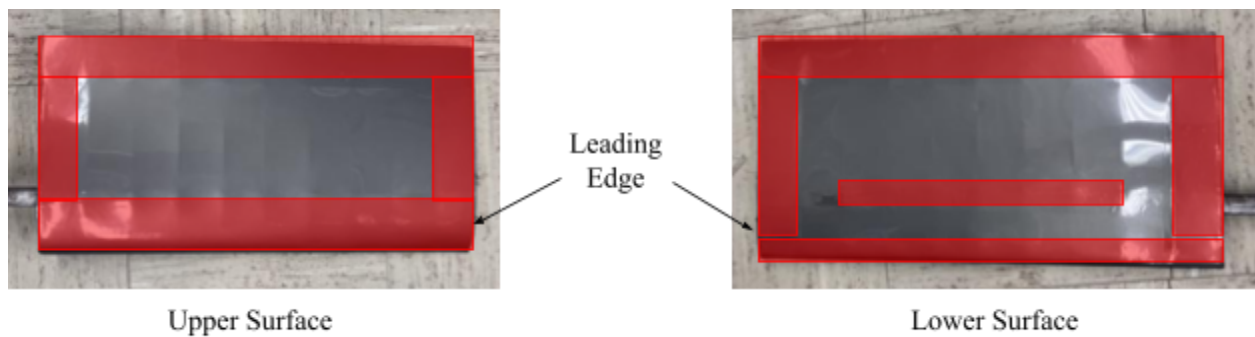


Figure B.3: Balsa Sheet Structure in MonoKote Wing

Despite its own imperfections, the balsa and MonoKote wing was able to conform better to the original specifications of the test article design compared to the composite prototype. Therefore, we went on to characterize the performance of the MonoKote wing against expected performance. If this project were to be continued, we would attempt another composite wing with our gained experience and insight.

## Appendix C - Tilt Rotor Mechanism FEA Studies

Multiple FEA analyses were conducted to get a better understanding of the possible stresses that the tilt motor mechanism would experience during testing. By no means were these simulations all that was used to test the strength of the mechanism, but they were used to aid in the design process. Additional physical testing was conducted to account for the physical defects and other complexities the simulation is unable to account for. All simulations used Fusion 360 Simulation with tetrahedral meshing. This Appendix is broken down into two sections with first detailing the servo mount and the subsequent detailing the L bracket. All of these simulations indicated that our parts would not break during testing nor have a large deflection.

### Servo Mount:

The specific type of 1/16 in. thick aluminum metal used for the servo mount was not known, and therefore the generic aluminum properties provided by Fusion 360 were used. This resulted in a Young's modulus of 68.9 Megapascals (MPa), a yield strength of 275 MPa, and an ultimate tensile strength of . There was one fixed constraint applied to the model which was applied at the base of the servo mount where the mount connects to the wing. The one 15 N force (twice the expected force during testing) was applied to the mount's servo connection points. The constraint can be seen in the figure below indicated by the lock and the force load can be seen indicated by the blue arrows. The simulation was conducted in three different configurations corresponding to the three flight modes: vertical, transition, and cruise. Figure C.1 below shows both the deflection and stress for the transition simulation.

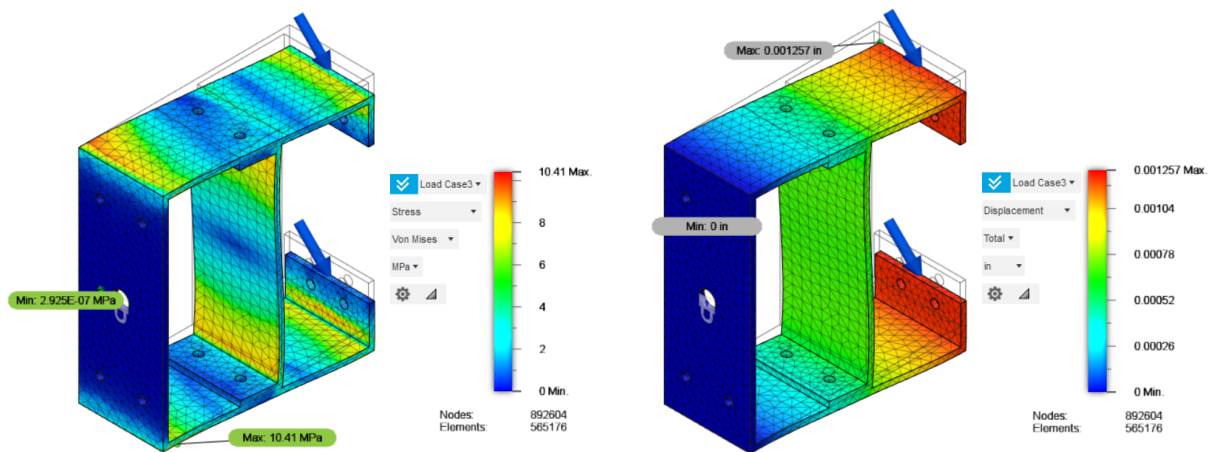


Figure C.1: FEA Transition Stress and Deflection Analysis of Servo Mount

By changing the force direction the three different flight modes were able to be simulated. This resulted in the following stress, displacement, and safety factor measurements in Table C.1 below.

Table C.1: Servo Mount FEA Results

Load Case	Max Stress (MPa)	Max Deflection (in.)	Minimum Safety Factor
Vertical Takeoff	3.3	$6.5 \times 10^{-5}$	83.6
Transition	10.4	$1.3 \times 10^{-3}$	26.5
Cruise	13.3	$1.8 \times 10^{-3}$	20.8

**L Bracket:**

The exact physical properties of the PLA filament used for the L bracket were not known and therefore the physical properties of the PLA plastic provided by Fusion 360 were used. This resulted in a Young’s modulus of 2.1 MPa, a yield strength of 26.9 MPa, and an ultimate tensile strength of 28.1 MPa. There was one fixed constraint applied to the model which was applied at the base of the L bracket where the bracket connects to the servo head. The one 15 N force (twice the expected force during testing) was applied to the mount’s motor connection points. The constraint can be seen in the figure below indicated by the lock and the force load can be seen indicated by the blue arrows. Unlike the servo mount, the simulation was conducted only in one orientation because the forces do not change regardless of direction. This resulted in a max stress 1.5 MPa which corresponds to a safety factor of roughly 18.6.

Moreover, the max deflection of this bracket is very small at  $5.7 \times 10^{-6}$  in. The deflection and stress of this simulation can be seen below in Figure C.2.

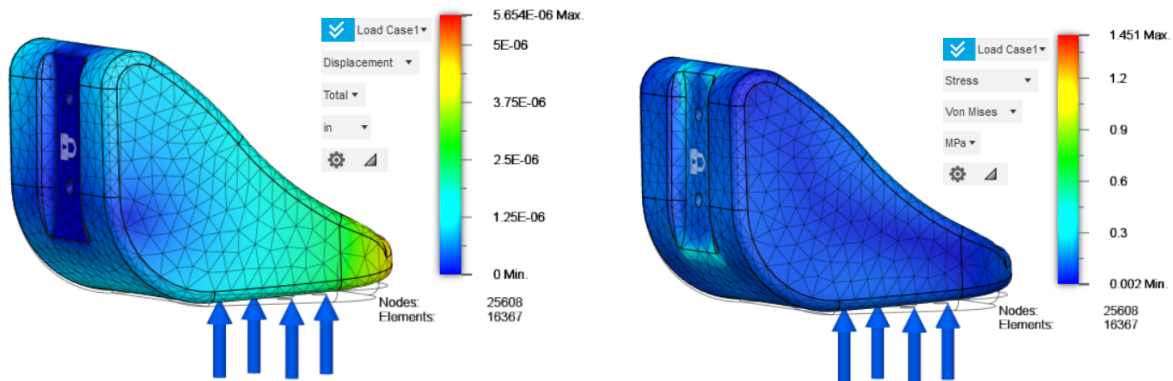


Figure C.2: FEA Transition Stress and Deflection Analysis of L Bracket

## Appendix D - Tilt Mechanism Software Code

```
#include <Servo.h>

// Set up both servo and motor to use the Servo.h library
Servo servo1;
Servo motor1;

// Create string to contain user input
String inputString;

// Set up pins for both servo and motor as well as motor PWM
int servoPin = 9;
int motorPin = 5;
int motorMinPWM = 1000;
int motorMaxPWM = 2000;

void setup() {

    // Attach the servo and motor to the corresponding pins
    servo1.attach(servoPin, 500, 2450);
    motor1.attach(motorPin);

    // Set servo and motor to their starting settings
    servo1.write(90);
    motor1.writeMicroseconds(0);

    // Start serial monitor
    Serial.begin(9600);
    analogReference(EXTERNAL);
}

void loop() {
    here:

    // Read in desired servo and motor inputs
    Serial.println("Input <servo in, motor in> to update:");
    while(inputString == "") {
        if (Serial.available() > 0) {
            inputString = Serial.readString();
            delay(15);
        }
    }

    // Determine indexes for end of both inputs
```



```

int cLoc = inputString.indexOf(",");
int bLoc = inputString.indexOf(">");

// Print error if servo input is more than four digits
if (cLoc > 4) {
    Serial.println("ERROR: INVALID SERVO INPUT");
    inputString = "";
    goto here;
}

// Pull inputs for servo and motor from string
int sInput = inputString.substring(1, cLoc).toInt();
int mInput = inputString.substring(cLoc + 2, bLoc).toInt();

// Print error if servo input is outside range
if (sInput < 0 or sInput > 270) {
    Serial.println("ERROR: INVALID SERVO INPUT");
    inputString = "";
    goto here;
}

// Print error if motor input is invalid percentage
if (mInput > 100 or mInput < 0) {
    Serial.println("ERROR: INVALID MOTOR INPUT");
    inputString = "";
    goto here;
}

// Print error if string is too long due to invalid input
if (inputString.length() > 10) {
    Serial.println("ERROR: INVALID INPUT");
    inputString = "";
    goto here;
}

// Map both inputs to correct values for writing
int sInMap = map(sInput, 0, 270, 0, 180);
int mInMap = map(mInput, 0, 100, motorMinPWM, motorMaxPWM);

// Rotate servo and print confirmation
servo1.write(sInMap);
Serial.print("Servo rotated to ");
Serial.print(sInput);
Serial.println(" degrees");

```

```
delay(50);

// Set motor to corresponding throttle and print confirmation
motor1.writeMicroseconds(mInMap);
Serial.print("Motor throttle set to ");
Serial.print(mInput);
Serial.println("%");

// Clear string used to read inputs
inputString = "";
}
```

## Appendix E - Phase 2 Pitot Probe Mounting Procedure

The placement of a second Pitot probe in addition to the existing probe in the 2 ft-by 2 ft wind tunnel was essential in recording exit airspeeds generated by the propeller-motor system. In order to accurately record the exit airspeeds generated by the propeller, the probe placement was dependent on distance behind the propeller. As the flow passes through the spinning propeller, it continues to accelerate for a select distance before momentum diffusion begins to occur. In consulting Professor Smith, it was determined that the second probe must be mounted at the location immediately before momentum diffusion began to occur. To find this location, airspeeds were recorded in 0.5 in. increments beginning 5 in. behind the propeller. The recorded exit airspeeds are shown in Figure E.1 below.

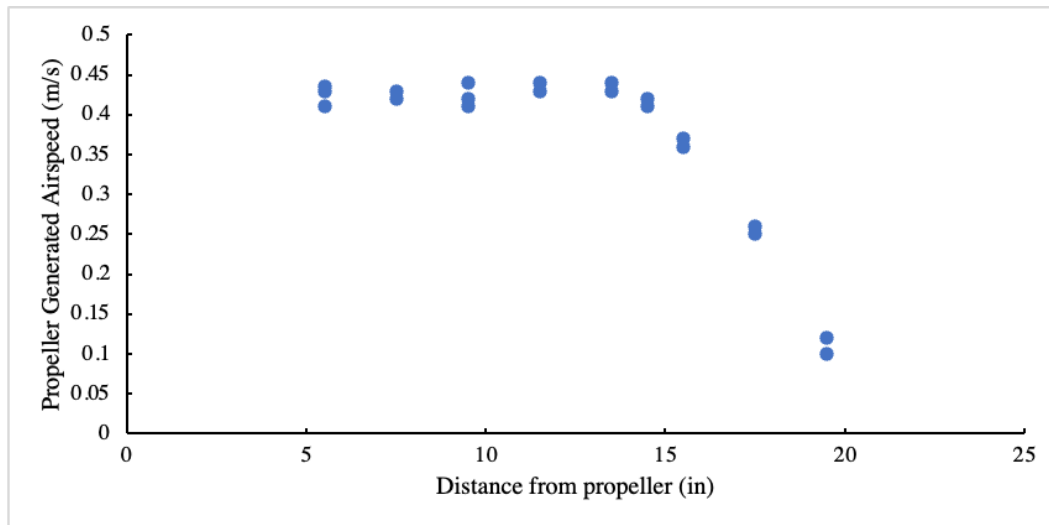


Figure E.1: Exit Airspeeds Behind the Propeller-Motor System

In Figure E.1 above, it is evident that momentum diffusion begins to occur after 13.5 in. behind the propeller. Therefore, the second probe was mounted at 13.5 in. behind the propeller to ensure accurate results for Phase 2 testing.

## Appendix F - Wing Performance Testing Raw Data

Table F.1: Wing Performance Testing Raw Data (5 m/s)

$\alpha$ (°)	$C_L$ Mean	$C_L$ Standard Error	$C_D$ Mean	$C_D$ Standard Error	$C_M$ Mean	$C_M$ Standard Error
-14	-0.3143555	0.0011116	1.9239142	0.0759914	0.0565099	0.0020365
-13	-0.3442244	0.0115544	1.8308091	0.0325955	0.0466580	0.0021771
-12	-0.3259775	0.0224798	1.4619151	0.1028875	0.0382867	0.0005756
-11	-0.3273861	0.0103066	1.4569675	0.0567362	0.0289805	0.0016726
-10	-0.2984357	0.0162373	1.3119192	0.0605178	0.0193608	0.0015036
-9	-0.2457139	0.0177743	1.1657282	0.0836250	0.0086475	0.0032070
-8	-0.2378213	0.0083572	1.1159718	0.0617598	-0.0027390	0.0019682
-6	-0.1840349	0.0121366	0.8711965	0.0720012	-0.0122081	0.0008984
-4	-0.1449998	0.0101688	0.7693102	0.0278186	-0.0099242	0.0012150
-2	-0.0907615	0.0079705	0.7581553	0.1487822	-0.0085225	0.0005054
0	0.0174843	0.0202647	0.3945996	0.1423932	-0.0032584	0.0021437
2	0.1010769	0.0148262	0.5163269	0.0519134	-0.0027627	0.0048985
4	0.1761359	0.0146663	0.6250621	0.0221488	0.0034638	0.0058255
6	0.2630646	0.0109172	0.6180819	0.0380439	-0.0103107	0.0019225
8	0.3641972	0.0081361	0.8264719	0.0208521	-0.0112330	0.0023806
10	0.3783825	0.0234800	0.7870993	0.0430686	-0.0055030	0.0018203
12	0.4936289	0.0168014	0.9240690	0.0289523	0.0005160	0.0021510
14	0.5564552	0.0118483	1.0212216	0.0964057	0.0004872	0.0012425
15	0.6107575	0.0168213	1.1461100	0.0275130	0.0024269	0.0000589
16	0.6856055	0.0200469	1.2235784	0.0270114	0.0062055	0.0006400
17	0.7324820	0.0206566	1.3640662	0.0531100	0.0018631	0.0005395
18	0.7556425	0.0043877	1.4724692	0.0150093	0.0006040	0.0005230
19	0.7856048	0.0338944	1.5796306	0.0832651	0.0025303	0.0008844
20	0.8475921	0.0071865	1.7386717	0.1171654	-0.0126293	0.0084440
21	0.8297522	0.0359434	1.8816003	0.0929181	-0.0138207	0.0091145
22	0.7727431	0.0156839	1.8522251	0.0104219	-0.0025592	0.0018096

Table F.2: Wing Performance Testing Raw Data (10 m/s)

$\alpha$ (°)	$C_L$ Mean	$C_L$ Standard Error	$C_D$ Mean	$C_D$ Standard Error	$C_M$ Mean	$C_M$ Standard Error
-15	-0.5082969	0.0002279	2.7173102	0.0399110	0.0665387	0.0005471
-14	-0.5263703	0.0074465	2.6946187	0.0212906	0.0621024	0.0004238
-13	-0.5443419	0.0064100	2.4221364	0.0110957	0.0496752	0.0016737
-12	-0.5259119	0.0079039	2.3086546	0.0260198	0.0419288	0.0003464
-11	-0.4932628	0.0062172	2.1273639	0.0125188	0.0343207	0.0006971
-10	-0.4629510	0.0016868	1.8848149	0.0150384	0.0196968	0.0013186
-9	-0.4242609	0.0043804	1.6693349	0.0269037	0.0034265	0.0005689
-8	-0.3877386	0.0017397	1.4678075	0.0260891	-0.0131799	0.0002202
-6	-0.2818634	0.0045276	1.1498344	0.0177747	-0.0176474	0.0010123
-4	-0.1962961	0.0075685	1.0655770	0.0230885	-0.0137703	0.0009082
-2	-0.1180911	0.0049627	1.0078499	0.0174617	-0.0114599	0.0008463
0	-0.0205315	0.0021567	1.0283690	0.0066122	-0.0018764	0.0025988
2	0.0572369	0.0187931	1.0446452	0.0077509	-0.0056846	0.0029613
4	0.1920331	0.0012017	1.0238118	0.0218831	-0.0016733	0.0021476
6	0.2846995	0.0069700	1.0307067	0.0072088	-0.0009464	0.0008126
8	0.3840355	0.0015878	1.0845584	0.0305180	0.0020691	0.0005346
10	0.4856571	0.0053960	1.1309498	0.0276630	0.0043669	0.0007164
12	0.5947564	0.0045021	1.1797002	0.0293233	0.0067793	0.0001425
14	0.7037008	0.0113513	1.2957916	0.0100802	0.0085677	0.0001995
15	0.7814191	0.0026214	1.4664148	0.0136532	0.0065602	0.0015689
16	0.8363613	0.0054689	1.5965640	0.0094530	0.0058559	0.0018383
17	0.8951331	0.0055959	1.8017309	0.0243560	0.0059198	0.0014386
18	0.8534510	0.0662505	1.8895296	0.0323438	0.0057917	0.0017677
19	0.8584745	0.0700414	2.1508350	0.1412496	-0.0134667	0.0146152
20	0.9057442	0.0897965	2.3845315	0.1470107	-0.0334918	0.0173891
21	0.9050422	0.1020498	2.5316571	0.0978914	-0.0369794	0.0181114
22	0.9088230	0.1090105	2.7031920	0.1329928	-0.0352220	0.0189635
23	0.7214387	0.0064445	2.8831861	0.1610040	-0.0381591	0.0275296

Table F.3: Wing Performance Testing Raw Data (15 m/s)

$\alpha$ (°)	$C_L$ Mean	$C_L$ Standard Error	$C_D$ Mean	$C_D$ Standard Error	$C_M$ Mean	$C_M$ Standard Error
-15	-0.6441708	0.0012094	3.3993376	0.0026192	0.0727176	0.0000143
-14	-0.6334703	0.0042588	3.1859529	0.0217378	0.0633853	0.0008960
-13	-0.6352491	0.0013786	2.9839164	0.0089023	0.0525562	0.0002289
-12	-0.6200623	0.0048896	2.7842299	0.0121668	0.0408003	0.0003527
-11	-0.5993534	0.0020799	2.6107399	0.0095065	0.0294077	0.0002518
-10	-0.5573635	0.0014222	2.3480728	0.0177824	0.0152832	0.0006110
-9	-0.5133938	0.0026886	2.0883912	0.0060970	-0.0056848	0.0003381
-8	-0.4652033	0.0058200	1.8088358	0.0101794	-0.0193357	0.0002662
-6	-0.3309551	0.0043334	1.5011236	0.0095826	-0.0189682	0.0001979
-4	-0.2485240	0.0012608	1.3928747	0.0081345	-0.0164631	0.0001591
-2	-0.1511723	0.0034138	1.3529777	0.0059158	-0.0118995	0.0002685
0	-0.0503322	0.0041344	1.3041825	0.0139585	-0.0083151	0.0004438
2	0.0615314	0.0014950	1.3018052	0.0174869	-0.0031255	0.0006867
4	0.1884538	0.0035992	1.3178883	0.0127855	-0.0026851	0.0002754
6	0.2969622	0.0054403	1.2993347	0.0097941	-0.0009846	0.0001489
8	0.4118441	0.0038926	1.3577069	0.0234960	0.0017928	0.0001245
10	0.5012863	0.0029848	1.3939089	0.0182488	0.0041106	0.0000759
12	0.6348848	0.0069014	1.4653945	0.0184116	0.0047524	0.0004260
14	0.7708002	0.0008340	1.6027146	0.0426423	0.0047599	0.0002423
15	0.8366479	0.0063832	1.7582385	0.0612117	0.0043270	0.0002806
16	0.9028000	0.0091614	1.9245532	0.0312482	0.0030670	0.0002943
17	0.9650692	0.0056763	2.0633841	0.0459420	0.0019858	0.0002652
18	1.0279203	0.0045492	2.2031746	0.0377431	0.0009953	0.0004112
19	1.0909848	0.0039383	2.3243372	0.0278317	-0.0004550	0.0004334
20	0.9937113	0.0812326	2.4833781	0.0409902	-0.0422064	0.0194720
21	1.0181412	0.1111330	2.6461965	0.0435624	-0.0462202	0.0210096
22	1.0411365	0.1275683	3.1515190	0.1172271	-0.0502204	0.0227249
23	1.0469034	0.1367437	3.3104193	0.1062075	-0.0537131	0.0244753
24	0.7402487	0.0033650	3.7555260	0.0040731	-0.0983128	0.0001048

Table F.4: Wing Performance Testing Raw Data (20 m/s)

$\alpha$ (°)	$C_L$ Mean	$C_L$ Standard Error	$C_D$ Mean	$C_D$ Standard Error	$C_M$ Mean	$C_M$ Standard Error
-15	-0.6827930	0.0046971	3.6342069	0.0093795	0.0743240	0.0002521
-14	-0.6851010	0.0029551	3.4523834	0.0121216	0.0654040	0.0006031
-13	-0.6853626	0.0026737	3.2425394	0.0168352	0.0536852	0.0005017
-12	-0.6710394	0.0019699	3.0242012	0.0055648	0.0388490	0.0008005
-11	-0.6357756	0.0011175	2.7869114	0.0098618	0.0255075	0.0002983
-10	-0.5922767	0.0022561	2.4866689	0.0121552	0.0081802	0.0002007
-9	-0.5496936	0.0010729	2.2574727	0.0095677	-0.0068744	0.0008160
-8	-0.4939912	0.0052783	2.0318906	0.0233180	-0.0195067	0.0010242
-6	-0.3808184	0.0004435	1.6551742	0.0086391	-0.0211195	0.0001432
-4	-0.2768339	0.0011365	1.5725387	0.0106794	-0.0175242	0.0000982
-2	-0.1728650	0.0015761	1.4925204	0.0205554	-0.0116356	0.0001215
0	-0.0595595	0.0013655	1.4772900	0.0037773	-0.0084598	0.0000830
2	0.0597326	0.0023610	1.4739032	0.0200567	-0.0047837	0.0001588
4	0.1673647	0.0014607	1.4731800	0.0212563	-0.0025803	0.0000689
6	0.2948275	0.0006267	1.4539137	0.0118267	-0.0013368	0.0000444
8	0.4079264	0.0063175	1.4944343	0.0142548	0.0014883	0.0001656
10	0.5230714	0.0038771	1.5553582	0.0121932	0.0038370	0.0000861
12	0.6452245	0.0020456	1.5923253	0.0182667	0.0044882	0.0001117
14	0.7850093	0.0023595	1.7174260	0.0423646	0.0044993	0.0001663
15	0.8556882	0.0045492	1.9001536	0.0620370	0.0036021	0.0000687
16	0.9325290	0.0049647	2.0835595	0.0266250	0.0024584	0.0001140
17	0.9861167	0.0046114	2.2254370	0.0360925	0.0016119	0.0000730
18	1.0547916	0.0068794	2.3754079	0.0356019	0.0006077	0.0001612
19	1.1188172	0.0111286	2.4832618	0.0408281	-0.0009589	0.0000829
20	1.1838105	0.0017552	2.6187944	0.0681453	-0.0023742	0.0001374
21	1.2376647	0.0058770	2.7957251	0.0550590	-0.0041433	0.0000896
22	1.0823210	0.1192756	2.9683637	0.0494871	-0.0546735	0.0244533
23	1.0947700	0.1391061	3.1357113	0.0517281	-0.0562851	0.0254204
24	1.0695671	0.1443183	3.6994208	0.1307318	-0.0651355	0.0207450
25	0.8520159	0.0489556	4.1714403	0.0068477	-0.1021847	0.0048994

## Appendix G - Airfoil Performance Simulation

To predict the performance of our wing section, we performed rudimentary simulations to predict the lift and drag characteristics of the airfoil. We performed the simulations in MFOIL, a tool developed by University of Michigan professor Krzysztof Fidkowski. In order to get the most accurate predictions, we performed the simulations at the Reynolds number that would match what our test article would experience in the wind tunnel. Our simulation results are shown in Figures G.1 and G.2 below:

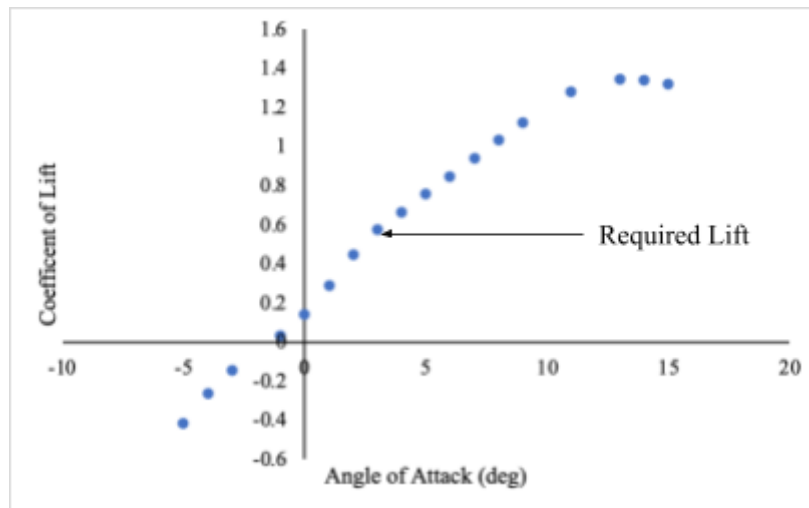


Figure G.1:  $C_L$  vs. Alpha for Simulated Airfoil

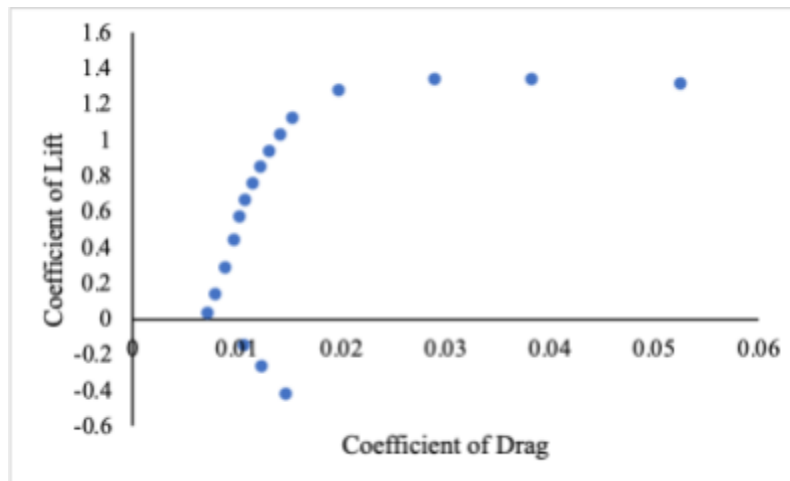


Figure G.2: Simulated Drag Polar

From our simulations, we would expect our wing to generate the required lift at cruise speed at  $4^\circ$  angle of attack. We were skeptical of the simulation results as there are limitations to the MFOIL program. First, we were only able to simulate a 2-D airfoil. This is limiting because 2-D evaluations underestimate drag since induced drag is absent. Another limiting factor is that viscous effects are not accounted for. Both these reasons cause our simulation to be inaccurate, but still worthwhile as they serve as a strong baseline for expected performance.



## Appendix H - Simulink Model State Space

This Appendix provides additional information regarding the state space model included in the Simulink model's plant. This state space computes both the horizontal and vertical forces using Newton's laws of motion. This model only considers the drone's motion in two directions because ideally a drone would not be moving laterally during transition. Moreover, this model does not include inviscid flow, exterior wind gusts, nor compressible flow. The Appendix is broken down into two sections, with one regarding the horizontal forces and the other detailing the vertical forces.

### Horizontal Forces:

The drone experiences only two horizontal forces: drag from the wing and the propeller's horizontal thrust component. This then allows  $F = ma$  to be rearranged to produce the following equation below. In this equation  $x_{acc}$  is drone's horizontal acceleration,  $m$  is the drone's mass,  $T$  is the propeller's thrust,  $AoT$  is the servo's angle of tilt,  $\rho$  is the air density,  $v_x$  is the horizontal velocity,  $S$  is the wing area, and  $C_{d_x}$  is the drone's horizontal coefficient of drag.

$$x_{acc} = \frac{1}{m} (T \cos(AoT) - \frac{1}{2} \rho v_x^2 S C_{d_x}) \quad (2)$$

### Vertical Forces:

The drone experiences four vertical forces: wing lift, vertical drag, weight, and propeller thrust. Similarly to the horizontal forces,  $F = ma$  was rearranged to produce the following equation below. All of the applicable coefficients previously defined in the horizontal forces equation above still apply to the vertical equation below. Additionally, this equations includes  $y_{acc}$  is drone's vertical acceleration,  $C_l$  which is the wing's coefficient of lift at a given angle of attack,  $g$  which is the gravitational constant,  $v_y$  which is the vertical velocity, and  $C_{d_y}$  which is the drone's vertical coefficient of drag.

$$y_{acc} = \frac{1}{m} (T \sin(AOT) + \frac{1}{2} \rho v_x^2 S C_l - mg - \frac{1}{2} \rho v_y^2 S C_{d_y}) \quad (3)$$

## Appendix I - Step Function Transition Profiles

This appendix overviews step function tilt profiles and explains why they are not ideal for our client's VTOL drone. Similarly to the initial slope causing a power peak discussed in Section 6.2.1, step functions will always result in power peaks. This concept is actually amplified by step functions because the tilt angle change in step functions is very quick and each step results in its own power peak. Ultimately, this is not ideal for the transition profile because it results in very quick and intense power changes which adds unnecessary complexity to the drone's transition. This can be seen in the Figure below which shows the tilt and power profiles for a step function transition occurring over an 8 second duration with 11.25° steps. The last 11.25° transitions linearly to allow for the drone to reach cruise speed.

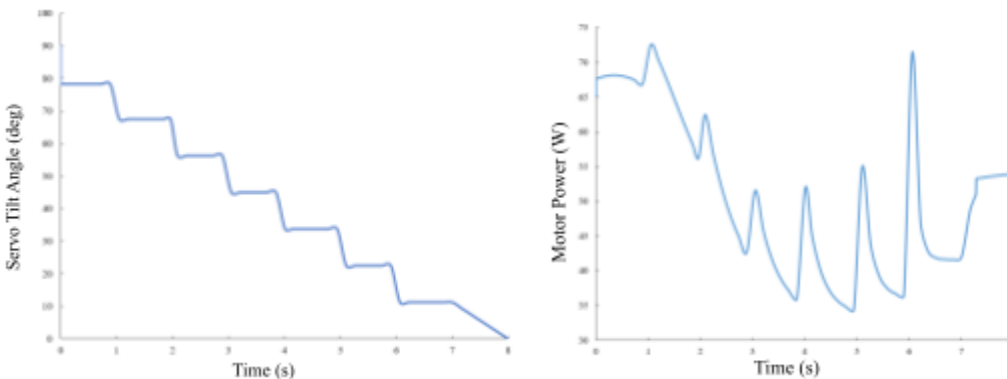


Figure I.1: Simulated Step Profile Tilt and Power Profiles

Even with the power peaks, the step profile above consumes a total amount of power that is comparable to the other profiles, but still not better than the linear profile. However, it is worth noting that there are more aggressive step profiles, such as the one shown below, that use less total power than the linear profile, but they result in much greater power peaks. Furthermore, these aggressive step profiles are only using less total power because they are benefiting from a low power consumption cruise for most of their transition which essentially equates to transitioning in a shorter period of time. This can be seen in the 8 seconds tilt profile below where the drone quickly tilts its motors to 45° and then 35° but then completes the last 35° of rotation in the last second.

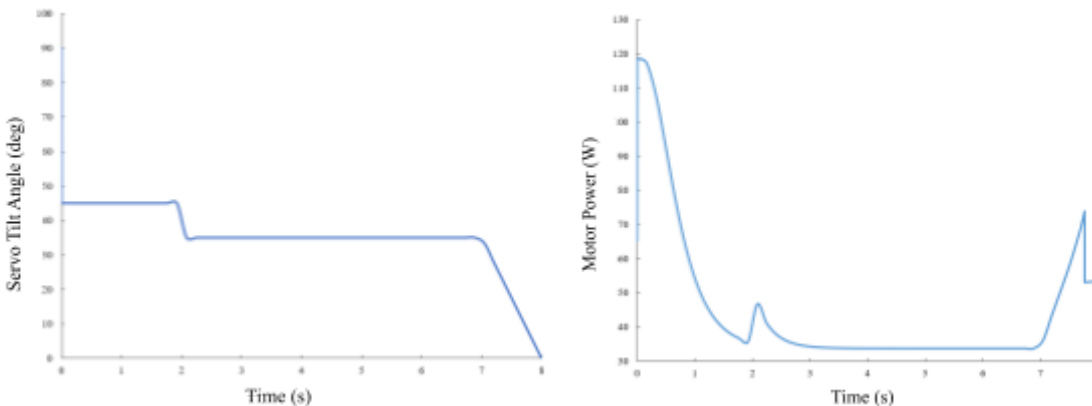


Figure I.2: Simulated Intense Step Profile Tilt and Power Profiles

By quickly transitioning over large steps at the beginning and end of the transition, this profile can consume 12% less total power than the linear profile, but at the trade-off of having a peak power 72% greater. During these quick tilt changes, the power needs to increase significantly, but it can remain low throughout the rest of the transition. While the drone is maintaining the 35° tilt angle from 2 to 7 seconds the power consumption can be seen to be very low. Throughout this time, the drone is actually not gaining horizontal velocity and is essentially cruising in a low power cruise configuration that ultimately allows this profile to consume less total power. So although it is true that this step function consumes the least amount of total power, it really only does so by transitioning in a shorter duration and flying in a low power consumption mode for the rest of the 8 seconds transition. So therefore, if a drone did have the power capabilities of reaching the maximum peak power required of the step functions, it would still make more sense to just conduct a linear transition in a shorter amount of time. The relationship between transition duration and maximum peak power for linear profiles is an idea more fully explained in Section 6.2.2.

Due to the reasons discussed above, our team has determined that step functions are not ideal for our client's drone. Using step profiles can reduce the total power consumption, but they significantly increase the maximum peak power. Moreover, shorter duration linear profiles provide the same total power consumption and maximum peak power trade-off without the additional power profile complexity.

## Appendix J - Changing Slope Transition Profiles

This Appendix is broken down into two sections with first detailing a concave up slope change and the subsequent detailing a concave down slope change.

### Concave Up Slope Change:

Changing the servo rotation rate to a slower rate throughout the transition results in the transition length being unjustifiably extended and an overall increase in overall power consumption when compared to a linear profile. This idea can be seen in the 8 seconds transition profile below where the rotation rate changes from  $15^\circ/\text{s}$  to  $7.5^\circ$  per second. When compared to the linear profile, this profile not only increases the peak power because now the initial rotation slope is greater, but also increases the overall power consumption due to the decreased slope near the end of the transition. Due to both of these reasons, concave up profiles are not ideal.

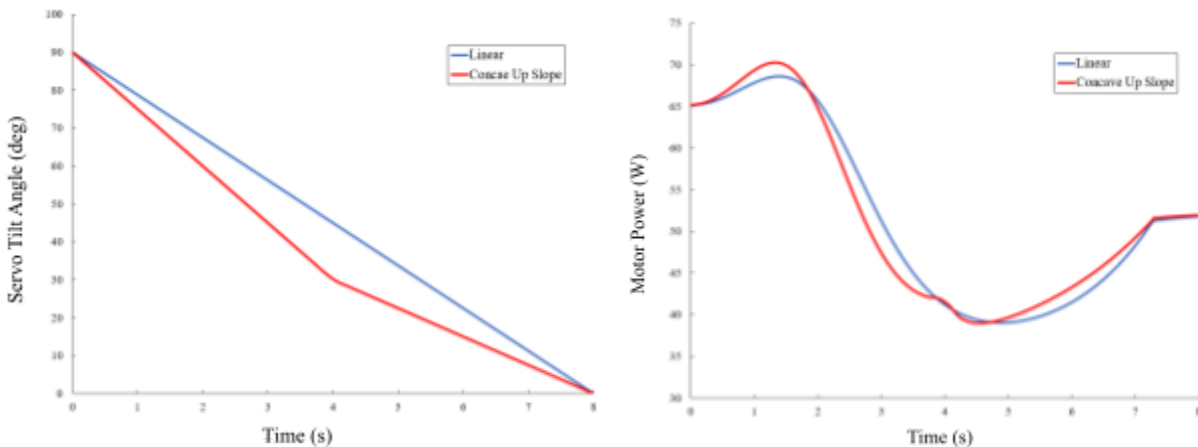


Figure J.1: Simulated Concave Up Slope Change vs Linear

### Concave Down Slope Change:

Increasing the rate of servo rotation throughout the transition results in the drone having to spend more time with its motors oriented near VTOL which results in increased power consumption at the start of the transition and less time to build horizontal velocity throughout the transition. This idea can be seen in the 8 second transition profile below where the rotation rate changes from  $7.5^\circ$  per second to  $15^\circ$  per second. When compared to the linear profile, this profile decreases the peak power because the initial rotation slope is less, but increases the overall power consumption due to the initial peak being stretched out horizontally from the decreased rotation rate. Due to the increased overall power consumption, concave down profiles are not ideal.

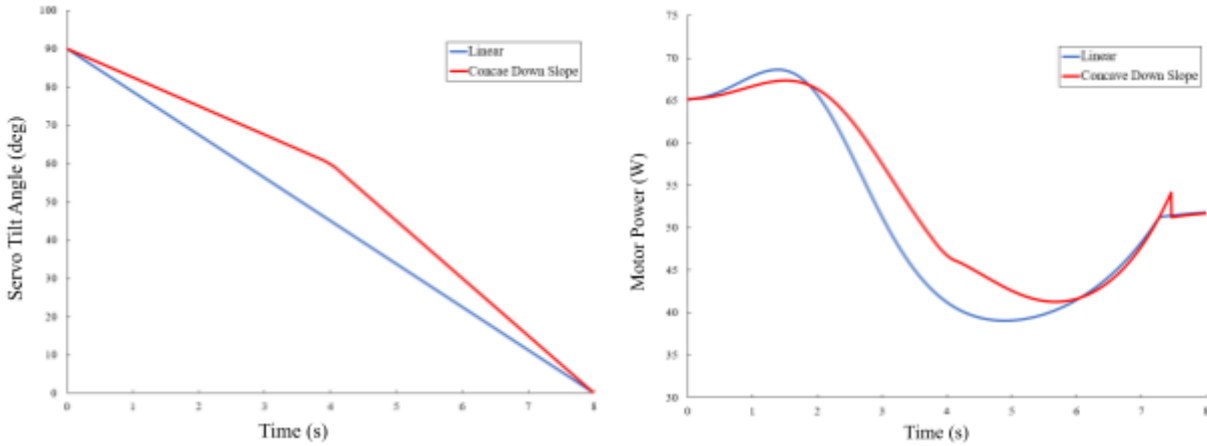


Figure J.2: Simulated Concave Down Slope Change vs Linear

The results shown above and on the previous page, indicate that the linear profile is better than both the concave up and down slope changing functions. Additionally, the same reasoning and results can be said about the negative square and positive square profiles shown in Section 6.2.1 as they follow similar paths to the concave up and down slope changing functions.

## Appendix K - Complete State Space of 8 Second Linear Transition

This figure below shows the complete state space outputs for the 8 second linear transition with the 2 second vertical takeoff before and the 2 second cruise after. This state space shows the similar tilt profiles and power profiles seen before, but it also shows the thrust, velocities, and positions. The horizontal velocity can be seen to increase almost logarithmically maxing out at its cruise velocity. This then results in the horizontal position increasing almost linearly. For the vertical velocity and position, both of these states can be seen to remain fairly constant throughout the simulation. There is a negative vertical velocity at the end of transition but this is due to rounding errors in the simulation and ultimately is a very small magnitude ultimately resulting in less than 0.1 m in altitude change. The power profile aligns with the previously shown profiles in Section 6 and the total power can be seen to be increasing throughout the simulation.

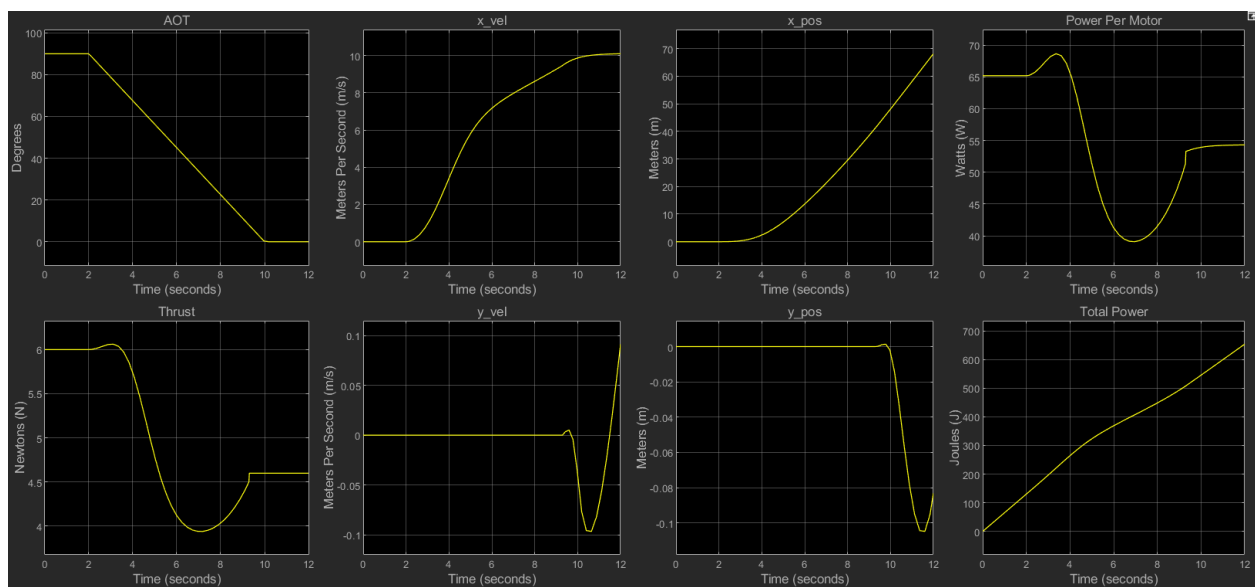


Figure K.1: Linear Transition Complete State Space

## Appendix L - Itemized Budget Breakdown

Table L.1: Itemized Budget Breakdown

Category	Item	Unit Cost (\$)	Proposed		Actual	
			Units	Cost (\$)	Units	Cost (\$)
Labor	Engineer	120/hr	400	48,000.00	707	84,840.00
	Consultant	50/hr	10	5,000.00	10	5,000.00
Facilities	Shop	50/day	8	400.00	10	5,000.00
	Wind Tunnel	60/day	6	360.00	5	300.00
Electronics	Motors/ESCs	50/ea	2	100.00	2*	0
	Servos	30/ea	2	60.00	1*	0
	Batteries	45/ea	1	45.00	2*	0
	BeagleBone	40/ea	1	40.00	1*	0
	Misc. Wiring	5/ea	1	5.00	4	39.52**
Materials	Polystyrene Foam	35/ea	2	70.00	0	0
	Metal	5/ea	2	10.00	1	18.99
	Wood	10/ea	1	10.00	9	92.63
	Misc. (Covering, glue, etc).	-	-	5.00	-	93.24
Hardware	Fasteners	1/ea	50	50.00	2	28.60
	Linkages	5/ea	2	10.00	0	0
	Motor Mount	5/ea	1	5.00	1*	0.00
Contingency				5,000.00	-	-
<b>Grand Total</b>				<b>54,640.00</b>		<b>86,412.98</b>

\*Provided in AE405 lab

\*\*Unit cost higher than anticipated

## References

- [1] Anthoine, J., Olivari, D., and Portugaels, D., "Wind-tunnel blockage effect on drag coefficient of circular cylinders," *Wind and Structures An International Journal*, vol. 12, 2009, pp. 541–551.
- [2] B. Li, J. Sun, W. Zhou, C. -Y. Wen, K. H. Low and C. -K. Chen, "Transition Optimization for a VTOL Tail-Sitter UAV," in *IEEE/ASME Transactions on Mechatronics*, vol. 25, no. 5, pp. 2534-2545, Oct. 2020, accessed 22 Jan. 2023, doi: 10.1109/TMECH.2020.2983255.  
<https://ieeexplore-ieee-org.proxy.lib.umich.edu/document/9051852>
- [3] Daniel P. Raymer. *Aircraft Design: A Conceptual Approach*. AIAA, 5th edition, 2012.
- [4] Ducard, Guillaume J.J. ; Allenspach, Mike. "Review of Designs and Flight Control Techniques of Hybrid and Convertible VTOL UAVs." *Aerospace Science and Technology*, vol. 118, Elsevier Masson SAS, pp. 107035-, accessed 22 Jan. 2023, doi:10.1016/j.ast.2021.107035.  
<https://doi-org.proxy.lib.umich.edu/10.1016/j.ast.2021.107035>
- [5] Liu, Zhenchang ; Guo, Jie ; Li, Mengting ; Tang, Shengjing ; Wang, Xiao. "VTOL UAV Transition Maneuver Using Incremental Nonlinear Dynamic Inversion." *International Journal of Aerospace Engineering*, vol. 2018, New York: Hindawi, pp. 1–19, accessed 22 Jan. 2023, doi:10.1155/2018/6315856.  
<https://go-gale-com.proxy.lib.umich.edu/ps/i.do?ty=as&v=2.1&u=umuser&it=DIourl&s=RELEVANCE&p=SCIC&qt=TI%7E%22VTOL+UAV+Transition+Maneuver+Using+Incremental+Nonlinear+Dynamic+Inversion%22%7E%7EPU%7E%22International+journal+of+aerospace+engineering.%22%7E%7ESN%7E1687-5966%7E%7ESN%7E1687-5974&lm=DA%7E1201811270000&sw=w>
- [6] Miller, T., *Composite Construction for Beginners*, CreateSpace Independent Publishing Platform, 2009.
- [7] Özgür Dündar, Mesut Bilici, Tarık Ünler, Design and performance analyses of a fixed wing battery VTOL UAV, *Engineering Science and Technology, an International Journal*, Volume 23, Issue 5, 2020, Pages 1182-1193, accessed 19 Jan. 2023, ISSN 2215-0986.  
<https://www.sciencedirect.com/science/article/pii/S2215098619316489>
- [8] Sun, H., Zhou, Z., Wang, Z., Dong, Q. (2023). Transition Strategy Optimization of Tilt-Rotor VTOL UAV in Conversion Process. In: Lee, S., Han, C., Choi, JY., Kim, S., Kim, J.H. (eds) *The Proceedings of the 2021 Asia-Pacific International Symposium on Aerospace Technology (APISAT 2021)*, Volume 2. APISAT 2021. *Lecture Notes in Electrical Engineering*, vol 913. Springer, Singapore. Accessed 19 Jan. 2023. [https://doi.org/10.1007/978-981-19-2635-8\\_78](https://doi.org/10.1007/978-981-19-2635-8_78)
- [9] Yuksek, B., Vuruskan, A., Ozdemir, U. et al. Transition Flight Modeling of a Fixed-Wing VTOL UAV. *J Intell Robot Syst* 84, 83–105 (2016). Accessed 19 Jan. 2023.  
[https://link.springer.com/article/10.1007/s10846-015-0325-9?utm\\_source=getftr&utm\\_medium=getftr&utm\\_campaign=getftr\\_pilot](https://link.springer.com/article/10.1007/s10846-015-0325-9?utm_source=getftr&utm_medium=getftr&utm_campaign=getftr_pilot)